The Relationship between Convectively Coupled Waves and the East Pacific ITCZ

FOUZIA FAHRIN,[a] ALEX O. GONZALEZ,[a,b] BRETT CHRISLER,[c] AND JUSTIN P. STACHNIK[c]

[a] *Department of Geological and Atmospheric Sciences, Iowa State University, Ames, Iowa*
[b] *Department of Physical Oceanography, Woods Hole Oceanographic Institution, Woods Hole, Massachusetts*
[c] *Department of Geography and Atmospheric Science, University of Kansas, Lawrence, Kansas*

(Manuscript received 3 July 2023, in final form 22 January 2024, accepted 31 January 2024)

ABSTRACT: Longstanding climate model biases in tropical precipitation exist over the east Pacific (EP) Ocean, especially during boreal winter and spring when models have excessive Southern Hemisphere (SH) precipitation near the intertropical convergence zone (ITCZ). In this study, we document the impact of convectively coupled waves (CCWs) on EP precipitation and the ITCZ using observations and reanalyses. We focus on the months when SH precipitation peaks in observations: February–April (FMA). CCWs explain 93% of total precipitation variance in the SH, nearly double the percent (48%) of the NH during FMA. However, we note that these percentages are inflated as they inevitably include the background variance. We further investigate the three leading high-frequency wave bands: mixed Rossby–gravity waves and tropical depression–type disturbances (MRG–TD type), Kelvin waves, and $n = 0$ eastward inertia–gravity waves (IG0). Compared to their warm pool counterparts, these three CCWs have a more zonally elongated and meridionally narrower precipitation structure with circulations that resemble past observational studies and/or shallow water theory. We quantify the contribution of all CCWs to four different daily ITCZ "states": Northern Hemisphere (NH) (nITCZ), SH (sITCZ), double (dITCZ), and equatorial (eITCZ) using a new precipitation-based ITCZ-state algorithm. We find that the percent of total precipitation variance explained by each of the CCWs is heightened for sITCZs and eITCZs and diminished for nITCZs. Last, we find that nITCZs are most prevalent weeks after strong CCW activity happens in the NH, whereas CCWs and sITCZs peak simultaneously in the SH.

SIGNIFICANCE STATEMENT: Convectively coupled atmospheric waves (CCWs) are a critical feature of tropical weather and are an important source of precipitation near the region of highest precipitation on Earth called the intertropical convergence zone (ITCZ). Given three decades of climate model biases in CCWs and ITCZ precipitation over the east Pacific (EP) Ocean during spring, few studies have examined the relationship between CCWs and the springtime EP ITCZ. We explored the CCWs and EP ITCZ relationship through calculations of the percent of precipitation that comes from CCWs. A significant portion of the tropical precipitation is associated with CCWs during spring. CCWs are even more impactful when the ITCZ is in the SH or on the equator, which are both problematic in climate models.

KEYWORDS: Intertropical convergence zone; Inertia-gravity waves; Kelvin waves; Atmospheric waves; Tropical variability

1. Introduction

A major proportion of global precipitation falls within the tropics, confined near the equator, where the northeasterly and southeasterly winds create a confluence zone called the intertropical convergence zone (ITCZ). The ITCZ represents the ascending branch of the Hadley circulation, which acts to balance Earth's energy by redistributing surplus heating to higher latitudes. It is well known that precipitation in the equatorial belt does not occur randomly but is often organized by large-scale convectively coupled waves (CCWs) within a few degrees of latitude of the ITCZ (Kiladis et al. 2009). We use the term "CCW" here, which encompasses convectively coupled Kelvin, equatorial Rossby (ER), mixed Rossby–gravity (MRG), $n = 0$ eastward inertia–gravity (IG0), and $n = 1$ inertia–gravity (IG1) waves (Blandford 1966; Matsuno 1966) as well as tropical depression (TD)-type disturbances (Takayabu and Nitta 1993) and the Madden–Julian oscillation (MJO; Madden and Julian 1971, 1972). We note that TD-type waves correspond to so-called easterly waves. Matsuno (1966) predicted the existence of all the waves mentioned above except the TD types and the MJO.

Due to the multiscale nature of CCWs in addition to their strong convective coupling, they continue to be severely misrepresented in Earth system models (Hung et al. 2013; Guo et al. 2015; Heath et al. 2021; Judt and Rios-Berrios 2021; Bartana et al. 2022). Hung et al. (2013) and Guo et al. (2015) showed that high-frequency CCWs (i.e., Kelvin, MRG, IG0, and IG1 waves) are generally too weak and low-frequency CCWs (i.e., ER waves and the MJO) are too strong in Earth system models, often referred to as being overly reddened at all scales including the power spectrum (Lin et al. 2006). At

Denotes content that is immediately available upon publication as open access.

Supplemental information related to this paper is available at the Journals Online website: https://doi.org/10.1175/JCLI-D-23-0398.s1.

Corresponding author: Fouzia Fahrin, ffahrin@iastate.edu

DOI: 10.1175/JCLI-D-23-0398.1

the same time, Earth system models have long suffered from tropical precipitation biases in the ITCZ, especially over the Atlantic and east-central Pacific Ocean basins, often referred to as the "double-ITCZ" bias (Mechoso et al. 1995; Lin 2007; Wang et al. 2015; Zhang et al. 2015; Adam et al. 2016; Si et al. 2021). In many models with double-ITCZ biases, there is too much precipitation in the Southern Hemisphere (SH) and not enough precipitation in the Northern Hemisphere (NH) during boreal winter and spring (Wang et al. 2015; Song and Zhang 2019). To what extent ITCZ precipitation variability can be explained by variability in CCWs, especially over regions such as the east Pacific (EP) Ocean and during months when ITCZ biases are largest, has yet to be fully explored.

The EP ITCZ is a particularly unique sector of the global ITCZ, with a relatively narrow region of zonally elongated clouds and precipitation that stays north of the equator most of the year and to the north of the strongest meridional sea surface temperature (SST) gradients (Yin and Albrecht 2000; Raymond et al. 2003; Wang and Magnusdottir 2006). However, during boreal spring [February–April (FMA)], the ITCZ recedes southward to its most equatorward position with relatively shallow convection (Huaman and Takahashi 2016), and often a second ITCZ appears in the SH. The presence of one ITCZ in each hemisphere is often referred to as a double ITCZ (Hubert et al. 1969; Zhang 2001; Gu et al. 2005). However, a double ITCZ does not occur consistently during FMA due to large subseasonal variability in ITCZ position (Henke et al. 2012; Haffke et al. 2016; Gonzalez et al. 2022) and strong interannual variability due to El Niño–Southern Oscillation (ENSO; Yang and Magnusdottir 2016). Due to these strong variations in ITCZ position during FMA over the EP and the documented relationships between CCWs and the ITCZ, the relationship between precipitation variability of the ITCZ and CCWs has been understudied and deserves further analysis.

Variability in the EP ITCZ can often be explained by undulations in its zonally elongated convection into convective systems that are associated with zonally propagating CCWs (Ferreira and Schubert 1997; Roundy and Frank 2004; Frank and Roundy 2006; Wang and Magnusdottir 2006; Kiladis et al. 2009; Huang and Huang 2011; Lubis and Jacobi 2015). Among all the CCWs, studies have observed that the influence of Kelvin waves on precipitation peaks over the EP near the equator during all months of the year (Roundy and Frank 2004; Frank and Roundy 2006; Kiladis et al. 2009; Huang and Huang 2011; Huaman et al. 2020; Cheng et al. 2022). Kim and Alexander (2013) analyzed the CCW variability using the Tropical Rainfall Measuring Mission dataset and showed that during March–April, the precipitation variances over the EP are dominated by westward-propagating high-frequency waves. Apart from these, Lubis and Jacobi (2015) documented that the combination of Kelvin, ER, TD type, and MRG waves contributed up to 20% of the total intraseasonal precipitation during November–April within 10°S–10°N in the EP.

Considering the highly variable ITCZ behavior in the EP during FMA, the goal of this study is to analyze the interaction between tropical precipitation and CCWs during those months. We hypothesize that CCWs explain a significantly higher percentage of the variance in SH convection over the EP, especially during boreal spring when SH precipitation is present in observations. We expect that certain configurations of the ITCZ (e.g., when precipitation is amplified south of the equator) are largely due to CCWs propagating into the region from South America or the west-central Pacific Ocean (Mapes et al. 2003; Mayta et al. 2021). To link CCWs to the ITCZ more directly, we develop a new, precipitation-based ITCZ identification algorithm on daily time scales that complements similar datasets created by Henke et al. (2012) and Haffke et al. (2016). Although there are numerous metrics used to diagnose changes in ITCZ position, width, and intensity (Byrne et al. 2018), such as zonally elongated clouds in satellite imagery (Wang and Magnusdottir 2006; Bain et al. 2011; Henke et al. 2012; Haffke et al. 2016) and boundary layer convergence maxima (Berry and Reeder 2014; Wodzicki and Rapp 2016; Weller et al. 2017), we focus on precipitation in this study because of its wide use in diagnosing both CCW and ITCZ biases.

The paper is organized as follows: the datasets and methods used are described in section 2, the results are presented in section 3, and last, the results are summarized in section 4. Comments regarding potential future work are also provided within section 4.

2. Data and methods

a. *Observational and reanalysis datasets*

Bilinear interpolated 1.0° × 1.0° daily accumulated precipitation rates were obtained from NASA's Integrated Multi-satellitE Retrievals for GPM (IMERG) for the years 2001–21 (Huffman et al. 2015). The interpolated grid spacing is coarser than the native output (0.1° × 0.1°) but is sufficient to capture the large-scale wave structure. For atmospheric dynamics fields such as geopotential heights, streamfunctions, and zonal and meridional wind, we used daily averaged 1.0° grid spaced data from the European Centre for Medium-Range Weather Forecasts (ECMWF) reanalysis, version 5 (ERA5), for 2001–21 (Hersbach et al. 2020). We eliminate the smoothed seasonal cycle from the ERA5 and IMERG anomalies by removing the first four harmonics at each grid point based on the daily climatology between 2001 and 2021.

b. *Wave-type filtering for CCWs*

We employ space–time spectral analysis on the IMERG daily precipitation anomalies following the general methods in Wheeler and Kiladis (1999). Regional (50°–170°W) spectra are produced by applying a Hann window that tapers the IMERG data using a cosine weighting from a maximum at the domain center (i.e., 110°W) to zero at the edges of the domain as done in Dias and Kiladis (2014). Furthermore, raw January through April (JFMA) spectra are produced one year at a time and then averaged over all years during the 2001–2021 time frame.

For each JFMA season (120 or 121 days total), three 80-day spectra are produced with 60-day successively overlapping segments for a total of three segments per season (i.e., days 1–80,

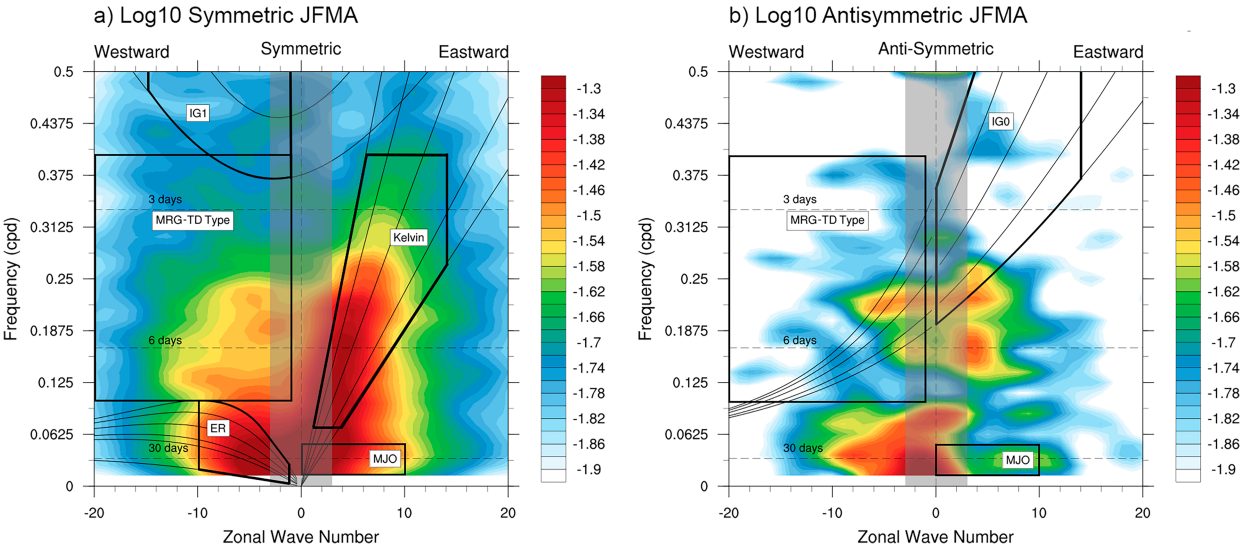

FIG. 1. Wavenumber–frequency power spectrum of the (a) symmetric and (b) antisymmetric components of IMERG precipitation anomalies for January through April 2001–21 over the EP (10°S–10°N, 50°–170°W). The dispersion curves for Kelvin, MRG, and IG0 waves are plotted for equivalent depths of 8, 12, 25, 50, and 90 m. For the ER wave, the dispersion curves are for equivalent depths 1, 8, 12, 25, 50, and 90 m. Last, for IG1, the curves are for depths 12 and 25 m. Heavy solid boxes indicate the wavenumber vs frequency filtering for each CCW used in this study (see Table 1). Gray shading indicates wavenumbers that are not fully resolved given the longitudinal trimming applied to calculate the regional power spectrum.

21–100, and 41–120). Unlike in Wheeler and Kiladis (1999), we do not divide by a smoothed background spectrum to identify statistically significant spectral peaks. This is done in part to reduce information loss, such as slow-moving Kelvin waves, that may occur when removing a smoothed background (e.g., Roundy 2020). Furthermore, examining the raw power spectrum eliminates potential ambiguities associated with the choice of background time scale (i.e., seasonal or annual). For example, dividing the JFMA spectra by the background for annual data would lower the significance of TD-type waves, given that these phenomena are associated with higher power in the boreal summer and are included in the year-round data (e.g., Hollis et al. 2023).

Figure 1 shows the 10°S–10°N average of the $\log_{10}$ of the symmetric and antisymmetric raw power spectra for JFMA 2001–21 over the EP (50°–170°W). It should be noted signals in low wavenumbers must be viewed with caution as we cannot fully resolve zonal wavenumber 3 or smaller due to our limited 50°–170°W domain. In the symmetric mode, the largest power is observed within the Kelvin wave dispersion lines followed by ER waves and in the MJO region. We also identify regions of enhanced power for westward traveling waves at higher frequencies that include our combined MRG–TD-type waves. For the antisymmetric mode, noticeable power appears within the dispersion curves for the combined MRG–TD-type waves and somewhat for IG0 waves.

A sensitivity analysis was performed using additional seasons to observe any differences in power within the analysis domain. For example, a seasonal analysis of July through October (JASO) from 15°S to 15°N showed differences from JFMA with a notable reduction of relative power within the Kelvin wave dispersion lines and less relative power in the ER and IG1 regions for the symmetric mode (Fig. 1a in the online supplemental material). The antisymmetric mode meanwhile showed stronger relative power within the middle of the combined MRG–TD-type region for JASO when compared to JFMA (supplemental Fig. 1b). Despite differences, we limit our analysis to the JFMA spectra when choosing boundaries to filter CCWs given our focus on the FMA ITCZ, which are identified in Table 1.

c. *Variance calculation*

The percent variance of total precipitation associated with each CCW filter wave band at a given point has been calculated to understand the CCW's influence on total precipitation. The variance calculation technique has been adopted from Schreck et al. (2013). The IMERG anomalies, already having their first four harmonics removed, are divided by their standard deviation (σ) at each grid point. The standardized anomalies are further filtered for the wavenumbers, frequencies, and equivalent depths associated with each wave-type

TABLE 1. Spectral window and equivalent depth used to filter CCWs.

Wave	Wavenumber	Period	Depth
Kelvin	1 to 14	2.5 to 14 days	8 to 90 m
IG0	0 to 14	0.5 to 5.3 days	8 to 90 m
MRG–TD type	−20 to −1	2.5 to 10 days	None
ER	−10 to −1	10 to 96 days	1 to 90 m
MJO	0 to 10	20 to 70 days	None
IG1	−15 to −1	0.5 to 3 days	12 to 50 m

filtering domain as described in Table 1. The variance with respect to the time dimension of the filtered data classifies as the fraction of the total precipitation variance associated with each wave-type filter band at each grid point. It is important to note that we must be careful while interpreting these values as they technically represent the fraction of the total variance that falls within a given wave filter domain and not simply the fraction of the total variance associated with a given wave type.

d. Lagged regression and estimates of wave properties

To produce the composite dynamical structure corresponding to the CCW-filtered precipitation, we applied lagged linear regression techniques from Wheeler et al. (2000) and Kiladis et al. (2009). For regression, we consider the whole FMA season instead of a time frame when the discrete signal of variance is present. The motivation behind this is that we are interested in quantifying the presence of CCWs over the entire season regardless of weak or strong signals. In doing so, we correlate and regress the space–time filtered anomalies of precipitation, horizontal winds, and either geopotential or streamfunction of a particular CCW band against its space–time filtered precipitation anomalies at a base point in each hemisphere. The base point is subjectively chosen where a significant amount of variance for the filtered CCW is present. The linear dependence of wind and precipitation anomalies with respect to the CCW anomalies are calculated using a 15 mm day^{-1} precipitation anomaly at our chosen base point. We estimate integer zonal wavenumber (K), phase velocity (C_p), and wave period (P) for each CCW by analyzing longitude plots of precipitation anomalies at the base-point latitude for each time lag. The integer zonal wavenumber is measured by first estimating the wavelength (λ) and using $K = (2\pi a\cos\phi)/\lambda$, where ϕ is the base-point latitude. The wavelength is estimated by taking the average zonal distance from the peaks of the wave at lag 0. The phase velocity is measured by taking the average zonal distance traveled by the peaks of the wave in 4 days for Kelvin waves and 2 days for IG0 and MRG–TD type and dividing it by the total number of days. To calculate wave period, we use the formula $P = 2\pi a/(C_pK)$, where a is Earth's radius. One point to make is all of the waves can be considered "wave packets" and composed of a combination of zonal wavenumbers because none of them are circumglobal.

e. Statistical significance

The wave-filtered precipitation and the dynamical fields for lag regression at our chosen base point are 95% significant. The statistical significance has been calculated at the $\alpha = 0.05$ level and is assessed at each grid point by using the field significance test of Wilks (2016), which accounts for spatial autocorrelation by controlling the false discovery rate. The method computes the latitude-weighted p value for all grid points, sorts them in ascending order, and sets a new threshold p value (p^*_{FDR}, in Wilks 2016) based on the distribution of p values. The local null hypotheses are rejected if the respective p values are smaller than the p^*_{FDR}.

TABLE 2. ITCZ-state decision table based on three precipitation metrics: (i) NH precipitation (pr_{NH}; 2°–20°N), (ii) equatorial precipitation (pr_{EQ}; 1°S–1°N), and (iii) SH precipitation (pr_{SH}; 2°–20°S).

pr_{NH}	pr_{EQ}	pr_{SH}	ITCZ state
Strong	Weak	Weak	nITCZ
Strong	Strong	Weak	nITCZ
Weak	Weak	Strong	sITCZ
Weak	Strong	Strong	sITCZ
Strong	Weak	Strong	dITCZ
Weak	Weak	Weak	aITCZ
Weak	Strong	Weak	eITCZ
Strong	Strong	Strong	eITCZ

f. Daily East Pacific ITCZ states

The latitudinal location of the ITCZ, or ITCZ state, over the EP Ocean region (20°S–20°N, 90°–135°W) is determined from daily IMERG precipitation. We adopt the same ITCZ states as in Haffke et al. (2016): double ITCZ (dITCZ), NH ITCZ (nITCZ), SH ITCZ (sITCZ), absent ITCZ (aITCZ), and equatorial ITCZ (eITCZ). We first apply a five-point running mean in the zonal direction to global IMERG precipitation data, which allows for better characterization of the ITCZ state on such short time scales. Note that no running mean is applied in time or in latitude, and this is critical for capturing what is often a latitudinally confined and highly transient ITCZ.

We analyze one longitudinal grid point at a time as a function of latitude to determine occurrences of ITCZ states over the entire longitudinal domain. From this, the most dominant ITCZ state is selected and applied for the entire domain for each daily time stamp. In a similar vein as Hwang and Frierson (2013) and Adam et al. (2016), we compute three latitudinally averaged precipitation metrics: (i) NH precipitation (pr_{NH}), (ii) equatorial precipitation (pr_{EQ}), and (iii) SH precipitation (pr_{SH}). Each of the three metrics is normalized by the 60th percentile of the 90°–135°W-averaged precipitation for that particular day. We use the 60th percentile as the normalized precipitation threshold because this allows for the closest spatial pattern and ITCZ-state percentage agreement with the Haffke et al. (2016) GridSat infrared (IR) satellite imagery ITCZ states, as will be seen in the results. Using the 70th percentile as the threshold yields an unrealistically large percentage of aITCZs and much smaller percentages of all other ITCZ states and vice versa for the 50th percentile. We determine whether each precipitation metric is "strong" or "weak" based on whether or not it is greater than or equal to 1. Table 2 shows the eight possible combinations of strong and weak designations for our three precipitation metrics.

One notable difference is expected between our precipitation-based ITCZ states and those from the GridSat infrared (IR) imagery algorithm of Henke et al. (2012) and Haffke et al. (2016). We define an absent ITCZ when the tropical precipitation signal is weak in all three of our precipitation metrics while Haffke et al. (2016) defines an absent ITCZ as when there is "no zonally organized convection zone on either

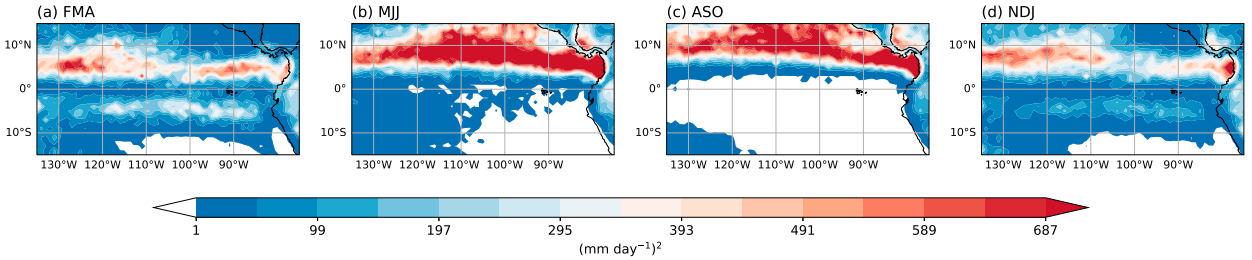

FIG. 2. Daily IMERG deseasonalized precipitation variance at 3-month intervals (2001–21) from 75° to 135°W. Variance less than 3 (mm day^{-1})^2 are omitted.

side of the equator." This implies strongly precipitating zonally asymmetric systems, such as CCWs, may be placed into the GridSat infrared (IR) imagery-based ITCZ-state algorithm as aITCZ but not in our precipitation-based ITCZ-state algorithm. We believe that this important distinction allows us to use our precipitation-based daily ITCZ states to more effectively document the relationship between CCWs and ITCZ states in this study.

3. Results

a. *Seasonal variability of CCWs over the eastern Pacific Ocean*

Figure 2 shows the spatial variability of deseasonalized precipitation variance over the EP for FMA, May–July (MJJ), August–October (ASO), and November–January (NDJ). During MJJ and ASO, the most intense and extensive precipitation activity occurs in the NH, away from the equator and north of 5°N (Bain et al. 2010; Haffke et al. 2016; Huaman and Schumacher 2018). The precipitation variance drops off during the NDJ season but remains relatively strong north of 5°N (supplemental Fig. 2). During NDJ and especially FMA, noticeable precipitation variance shows up south of the equator. At the same time, the NH precipitation variance weakens and moves equatorward. The southern branch of ITCZ is visible from February to May but it is most intense in March (supplemental Fig. 2). The existence of precipitation variance in both hemispheres during boreal spring represents the well-known double ITCZ of the EP (Zhang 2001; Gu et al. 2005; Huaman and Takahashi 2016).

Given that the deseasonalized precipitation variance is always smaller in the SH than in the NH, we focus on investigating the impact of CCW variance associated with any given filtered wave band during the FMA season, when the largest SH precipitation variance occurs. Before exclusively concentrating on the FMA season, we determine the season when most, if not all, filtered CCWs that fall within the frequency–wavenumber range defined by the filter band of the respective waves have the largest impact on the total precipitation variance through the percent or fractional variance (Schreck et al. 2013). One important caveat of the calculation is these fractional variances are overestimates of the true variance and that the variances explained by each wave filter band are strongly dependent on the size and location of each filter box. For example, boxes of equal frequency intervals will automatically have more variance at lower frequencies and wavenumbers due to the "redness" of the background spectrum in each wave domain.

Figure 3 shows the seasonal variation for the percent variance of each CCW filter band spatially averaged over 15°S–15°N and

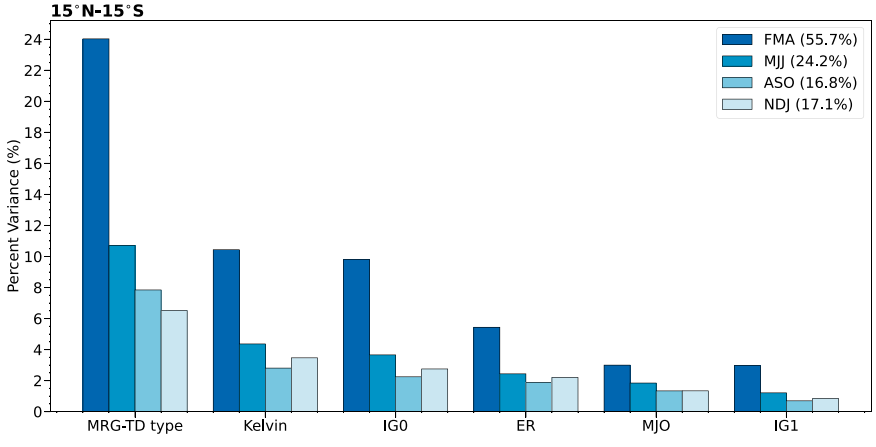

FIG. 3. Percent of total precipitation variance explained by the indicated filter bands of each wave type over the EP (75°–135°W) from 2001 to 2021 averaged between 15°N and 15°S during FMA, MJJ, ASO, and NDJ.

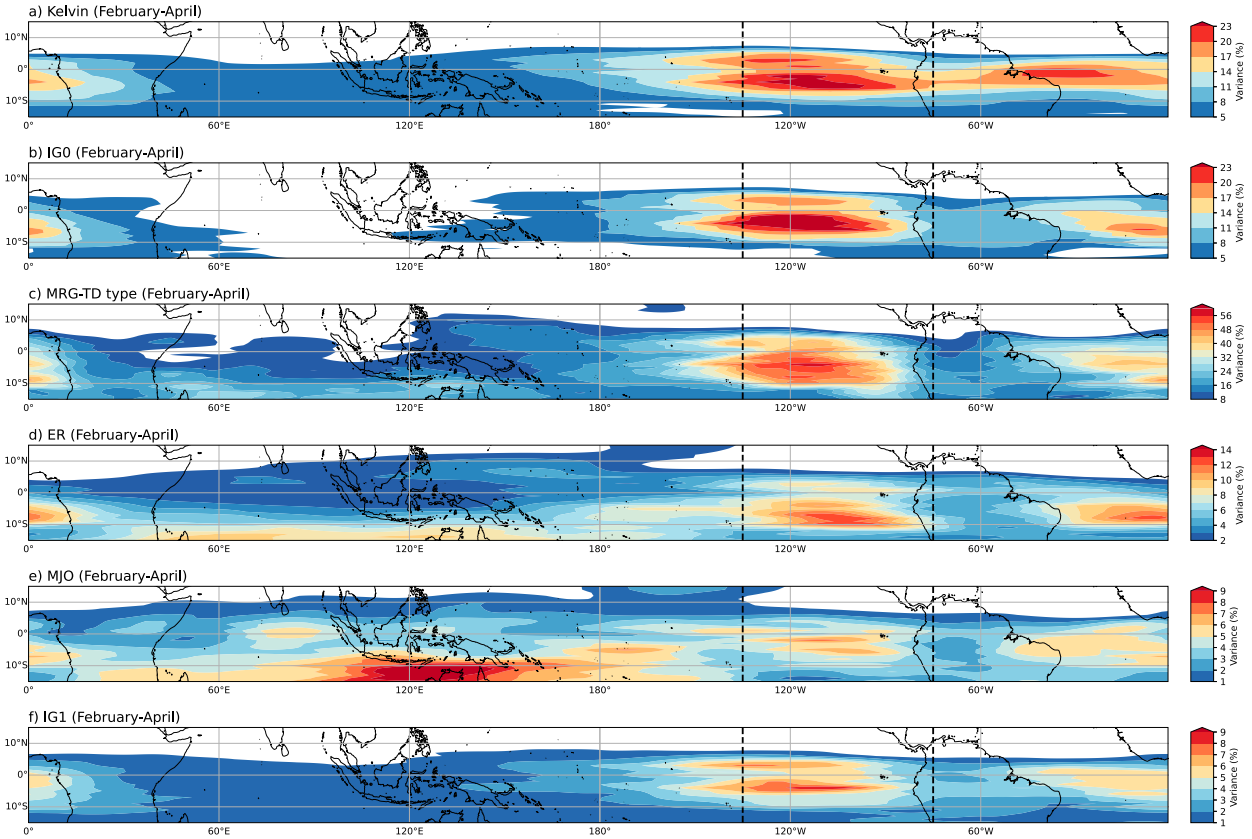

FIG. 4. Percent of total precipitation variance that falls within (a) Kelvin, (b) IG0, (c) MRG–TD type, (d) ER, (e) MJO, and (f) IG1 filtered wave band during FMA from 2001 through 2021. The black dashed lines enclose the EP region used in Fig. 3. Note the different scaling of the color bars.

75°–135°W. The seasonal cycles of all the waves are relatively similar in the EP in that they explain the most variance during FMA (55.7%; Fig. 3) and least during NDJ (17.1%; Fig. 3) or ASO (16.8%; Fig. 3). We infer that these results are likely due to the standard deviation of daily anomalous precipitation being larger in the NH than near the equator or in the SH.

The Kelvin filtered wave band has the maximum impact on precipitation during FMA (10.5%) and minimum impact during ASO (2.8%; Fig. 3), which is in broad agreement with total column precipitable water results from Roundy and Frank (2004). Kelvin wave activity from our results is roughly similar to Lubis and Jacobi (2015), where they used outgoing longwave radiation data to show that tropical precipitation is strongly impacted by Kelvin waves during boreal spring. In our results, during MJJ and ASO (extended boreal summer season), the combined percent variance explained by Kelvin filtered wave band is lower than NDJ and FMA (extended boreal winter) and shifts northward with little to no precipitation activity in the SH during later months (Lubis and Jacobi 2015). One possible explanation for the strongest percent precipitation activity over the EP occurring during boreal spring is because Kelvin wave activity is more equatorially trapped compared to most other CCWs and thus, it more readily follows the ITCZ when the ITCZ is near the equator in both hemispheres (Masunaga 2007; Kiladis et al. 2009; Huang and Huang 2011). In addition, during northern winter, some of the eastward Kelvin filtered variance is due to extratropical Rossby waves that intrude into the westerly duct (Huaman et al. 2020; Cheng et al. 2022).

The spatial distribution of percent variance associated with each CCW filtered band in Figs. 4a–f shows the influence of wave activities during FMA. Figure 5 involves NH versus SH spatial averaging of the FMA CCW filtered band percent variance over our focused EP region (75°–135°W). In Fig. 5, the tropics have been divided into a NH (0°–10°N) and SH (0°–10°S) region over the EP. Precipitation variability in the SH is dominated by CCWs, resulting in 93.3% of the total variance. Figures 4a–f, showing the spatial distribution of CCW filtered percent variance over the EP during FMA, support this notion in that the waves are far more active in the SH than the NH during FMA. At the same time, the map plots highlight the importance of CCW activity in the region just north of the equator but south of the main FMA precipitation band in Fig. 2a. The impact of Kelvin, IG0, and MRG–TD-type wave-band filtered precipitation on the total precipitation is predominantly higher than other wave bands in both hemispheres (Fig. 4). However, this is likely impacted by the large spectral size of their filter bands.

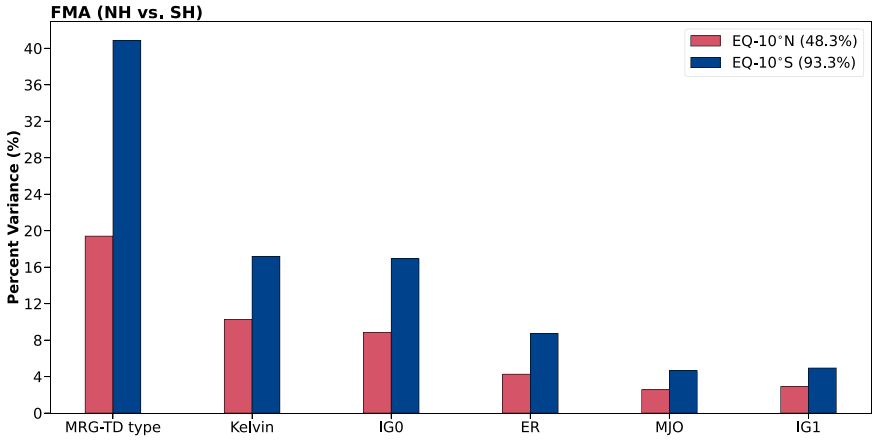

FIG. 5. Percent of total precipitation variance explained by each wave filter band over the EP (75°–135°W) from 2001 to 2021 averaged between 0°–10°N and 0°–10°S and for FMA denoted by the red and blue bars, respectively.

While Fig. 4d shows similar results for the ER wave band, the most enhanced ER wave influence is found in the SH away from the equator. During December–February, eastward and westward-propagating disturbances can be excited by extratropical Rossby waves, and the change in static stability due to the intrusion of high potential vorticity can excite equatorially trapped Rossby modes (Kiladis 1998). ER waves are most active during November–April in the Asian monsoon region and the southwestern Pacific Ocean (Lubis and Jacobi 2015) and thus not as potentially important to tropical precipitation over the EP as these other regions. At the same time, Fig. 3 shows that ER filtered wave bands contribute most strongly to fractional precipitation variance during FMA.

The IG0 filtered wave appears as one of the three most prominent CCWs in terms of the anomalous precipitation percent variance during FMA (Fig. 3); however, there are a limited number of studies on IG0 wave observations, partly because IG0 waves can propagate with accompanying MRG waves or other CCWs (Kiladis et al. 2016). Kiladis et al. (2016) used an empirical orthogonal function approach and found evidence that the MRG–IG0 activity is enhanced when there is minimum equatorial SST and a strong double ITCZ (Hendon and Liebmann 1991) while noting this pattern is disrupted during El Niño years. However, other studies have shown that MRG waves always have a weak impact on EP precipitation regardless of the season (Kiladis et al. 2009; Horinouchi 2013).

The contribution of the MRG–TD-type filtered wave band explains the greatest precipitation variance in all seasons (Fig. 3) and is more than twice as large in the SH as in the NH (Fig. 5). The profound activity of the MRG–TD-type wave band, especially in the SH, can be linked to the fact that TD-type disturbances are strongest when the most active ITCZ convection happens (Kiladis et al. 2009). Our results show the MRG–TD-type wave-band filtered variance is stronger away from the central American coast (Fig. 4c), which suggests that local east Pacific processes (e.g., ITCZ breakdown and the upscale growth of mesoscale convective systems) might play a role in exciting TD-type disturbances locally as the Atlantic Ocean connection is weaker (Mapes et al. 2003; Wang and Magnusdottir 2005). At the same time, given that tropical cyclogenesis does not occur during FMA, any tropical disturbances formed during FMA must be limited by unfavorable environmental conditions, such as cool SSTs or a dry low to midtroposphere. Moreover, Frank and Roundy (2006) found a weak relationship between MRG–TD wave activity and cyclone formation in the northeastern Pacific. These results give a possible explanation for the strongest MRG–TD-type filtered wave-band activity during FMA since we did not find such a feature of tropical cyclogenesis formation from the MRG–TD-type disturbances in section 3b.

The MJO and IG1 filtered waves show less precipitation activity during FMA (Figs. 3 and 4) likely due to their smaller spectral wave bands. IG1 filtered waves often propagate westward within the MJO envelope over the Indo-Pacific warm pool, and possibly that is why both have a relatively weak signal over the EP regardless of the season (Fig. 3) (Kiladis et al. 2009). The relatively enhanced MJO activity during FMA corresponds to the fact that MJO is far more active in the SH than in the NH (Frank and Roundy 2006). The MJO wave-filtered fractional variance shows different results from actual variance in Zhang and Dong (2004), where they found the MJO variance peaks during boreal summer over the EP. Other studies showed that MJO propagation from the western to EP is not continuous, and warmer SSTs along with weak mean zonal flow induce MJO activity during boreal summer (Knutson and Weickmann 1987; Maloney and Kiehl 2002; Zhang and Dong 2004).

b. Spatial and temporal variability of leading high frequency CCWs

In this section, the FMA time-lagged composite of precipitation and dynamical fields of the three leading high frequency CCWs (Kelvin, IG0, and MRG–TD-type) are analyzed. Together these waves explain the majority of the total CCW-filtered precipitation variance and we thus only present their composites in the

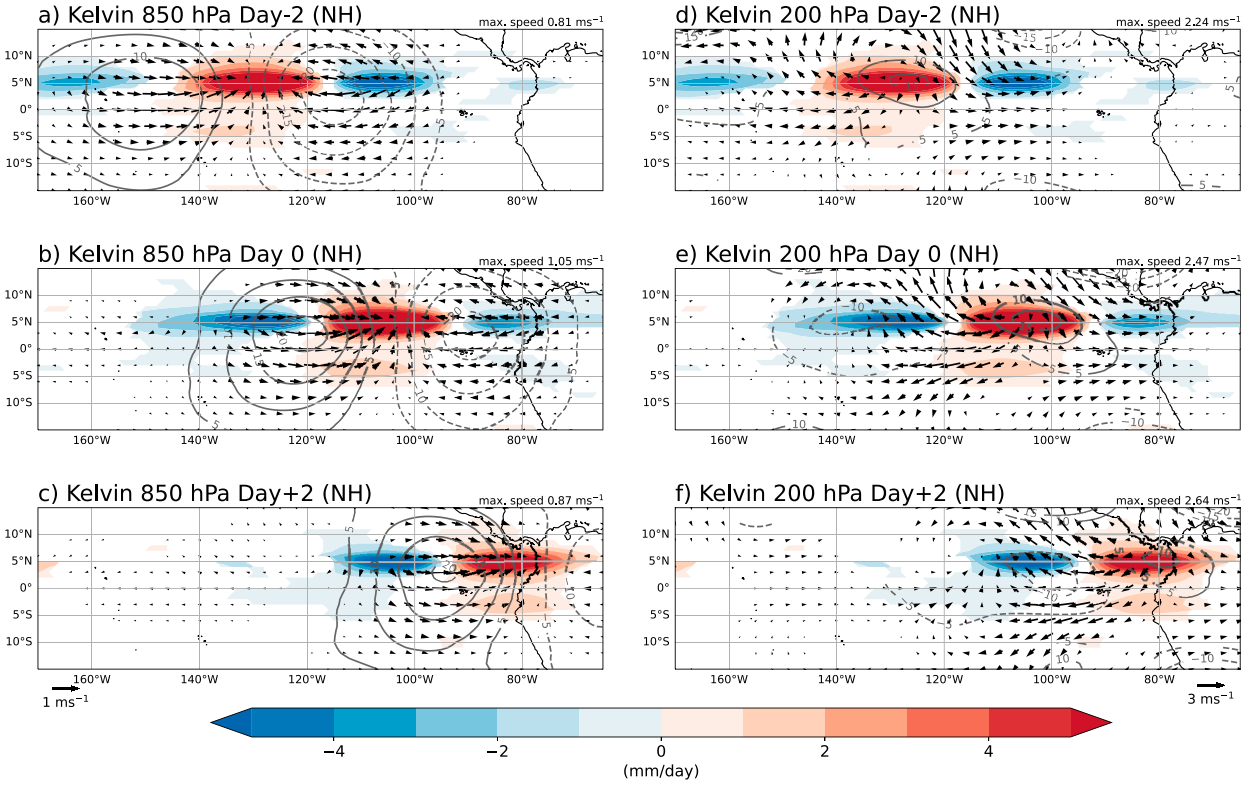

FIG. 6. Maps of Kelvin wave-band filtered precipitation (shading), geopotential height (contours) and wind (vectors) anomalies associated with the Kelvin wave-band filtered precipitation at the base point 5°N, 105°W for day −2, day 0, and day +2 for (a)–(c) 850 and (d)–(f) 200 hPa. Geopotential height contours start at ±25 m and the interval is 5 m with negative contours dashed. Shading and contours indicate regions significant at the 95% level. Wind vectors are plotted only where either the u or v component is significant at the 95% level or greater, with the largest wind vector as shown in the top-right corner. Every third vector is shown for readability.

following analysis. We note that the fraction variance calculation cautions in the last section apply much less to the regression approach used here since the assumption is that the background, although red, is truly random and should have minimal impact on the "signal" associated with the spectral peaks. Another motivation for further inspecting these three CCWs is that they are high-frequency CCWs highlighted as underestimated in Earth system models (Guo et al. 2015). Note that the other high-frequency CCW, IG1, is not analyzed further because its wave band is not fully captured in daily data (see Fig. 1).

1) KELVIN WAVES

Figure 6 shows the regressed precipitation anomalies, associated 850- and 200-hPa wind, and geopotential height at the NH base point (5°N, 105°W). Two days before the peak in convection, the positive precipitation anomaly signal is centered at about 130°W, and the precipitation and dynamical signals move eastward in subsequent lags. The wavenumber and phase velocity have been calculated following the methodology described in section 2d. In both hemispheres, the waves have an estimated zonal wavenumber of 6–7, phase velocity of approximately 17–18 m s^{-1}, and a period of approximately 4 days (0.25 cycles per day), which is consistent with the strong power shown in Fig. 1.

As anticipated based on equatorial wave theory (Matsuno 1966; Gill 1980), the horizontal winds at 850 hPa are mostly zonal at each of the three lags. On a broad scale, the lower tropospheric height and wind pattern have an in-phase relationship and are nearly symmetric about the equator similar to the theory (Kiladis et al. 2009). Heights are low with easterlies east of the maximum precipitation and high height with westerlies west of it as predicted by the theory (see Fig. 3f of Kiladis et al. 2009), even though the stronger convective portion of the wave is significantly north of the equator. This pattern of near symmetry of the dynamical fields about the equator associated with off-equatorial strong convective signal in NH is also seen in March–May (Huaman et al. 2020) and in June–August (Straub and Kiladis 2002, 2003). Close to the maximum positive precipitation anomalies, the meridional wind component becomes relatively large, and southerlies feed into the region of active convection primarily from the equatorial side. For the negative precipitation anomalies, we see relatively strong meridional divergence both on the poleward and equatorial sides. On day +2, the Kelvin wave reaches South America with strong west-southwesterlies near the maximum precipitation anomaly but little to no signal to the east as the topography acts as a barrier for convective and dynamical fields propagation (Matthews 2000). The Kelvin wave propagates slightly faster over the EP and slows down

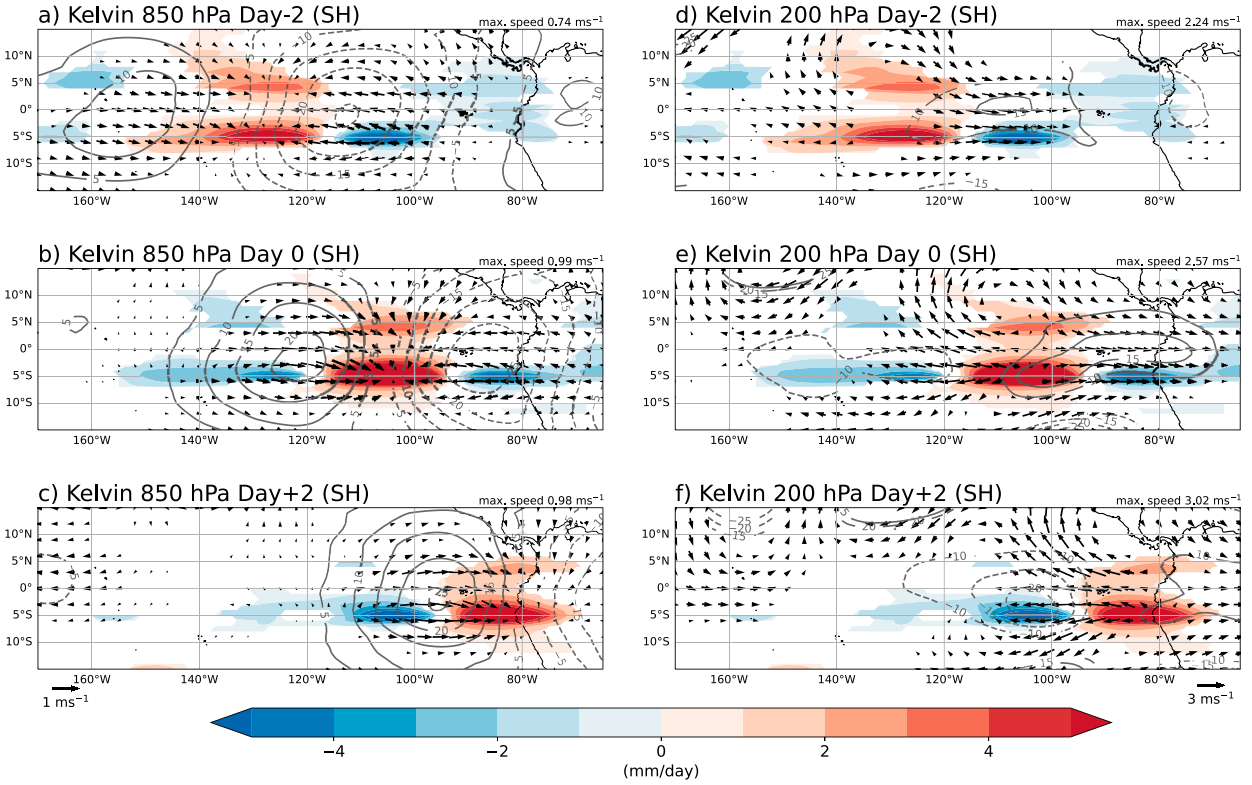

FIG. 7. As in Fig. 6, but for 5°S, 105°W.

as it reaches South America in later lags (not shown) because of strong convection associated with South America's topography (Mayta et al. 2021). The theoretical Kelvin wave on the equatorial β plane is encompassed entirely by a zonal component of wind, but in the real atmosphere, extratropical Rossby wave–like components can initiate a moist Kelvin wave coupling with a significant meridional wind component (Wang and Rui 1990; Straub and Kiladis 2002). The shape of the Kelvin wave convection is more zonally elongated and narrower in the EP compared to the warm pool (Straub and Kiladis 2002, 2003; Kiladis et al. 2009).

The dynamical fields associated with the Kelvin wave in the upper troposphere are slightly different from the shallow water (SW) mode (see Kiladis et al. 2009). Although strong divergence is present at 200 hPa, the height field is weaker than the lower troposphere. The zonal wind flow is south of the maximum precipitation and more prominent south of the equator, with easterly flow west of the precipitation maximum and westerly flow east of it. There is a substantial wind asymmetry about the equator present in contrast to the 850-hPa flow evident at each of the three time lags. The wind patterns in Figs. 6d–f have a cyclonic and anticyclonic circulation, which is more prominent north of the convection. Huaman et al. (2020) suggested that Kelvin waves and extratropical eastward-propagating disturbances may interact with each other if they occur at the same longitude. Since our study area confines 15°N–15°S, this extratropical–tropical connection is not entirely captured here. Nevertheless, there are twin anticyclones straddling the equator in both hemispheres (Fig. 6e) in the upper troposphere, which is consistent with Liebmann et al. (2009).

Moving to the SH base point (5°S, 105°W) in Fig. 7, while there is enhanced precipitation near the southern base point, the anomalous precipitation pattern is more symmetric about the equator than it is for the regressions at the NH base point. This precipitation pattern resembles more of a double-ITCZ structure deviating from the theoretical SW mode (Matsuno 1966; Kiladis et al. 2009). The relatively strong precipitation signal in the NH may be due to the warm background SST to the north of the equator (Straub and Kiladis 2002). At each of the three lags, the 850-hPa wind pattern and geopotential height field show a similar pattern as in NH (Figs. 6a–c), with slightly more symmetry about the equator. In the upper troposphere, divergence is mostly zonal near the maximum precipitation (Fig. 7e). However, the meridional component of wind maximizes north of the equator with a pair of cyclonic and anticyclonic vortices at day 0, highlighting the fact that the real atmosphere can have significant deviations from theoretical dynamical structure corresponding to the SW modes (Chao 2007).

2) $N = 0$ INERTIA–GRAVITY WAVES

While the same NH and SH base points have been used for lag regression of the convectively coupled IG0 wave, we only document precipitation anomalies and 850-hPa dynamical fields since the upper-tropospheric wind patterns do not have a widespread statistically significant response (not shown). The regressed IG0 fields at the NH and SH base-point plots have

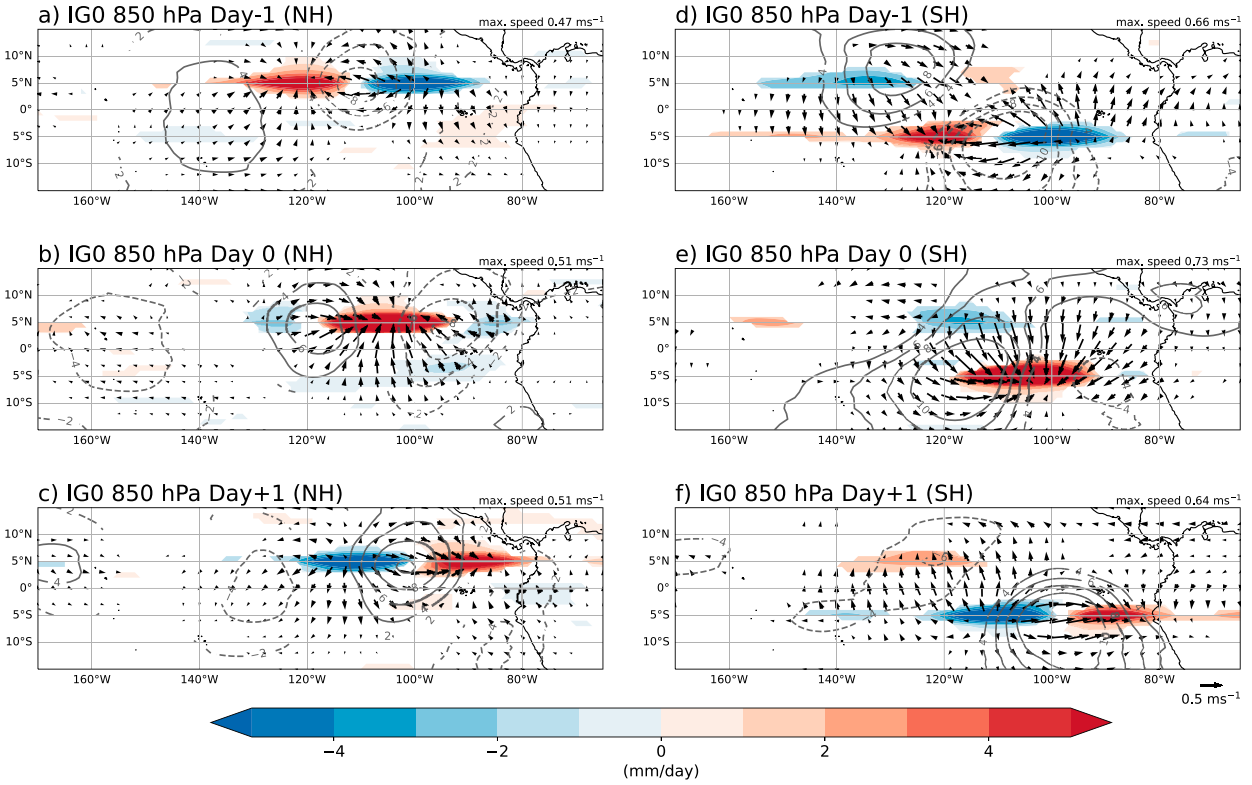

FIG. 8. As in Fig. 6, but for IG0 wave-band filtered precipitation anomalies at the base point (a)–(c) 5°N, 105°W and (d)–(f) 5°S, 105°W for day −1, day 0, and day +1 for 850 hPa. Geopotential height contours start at ±10 m and interval is 2 m with negative contours dashed.

an estimated zonal wavenumber of 8, an eastward phase propagation speed of approximately 22–23 m s^{-1}, and a wave period of approximately 2.5 days. At day −1 for both base points, but especially the SH base point (Fig. 8d), the precipitation anomalies broadly form a quadrupole resembling the divergent anomalies of the IG0 wave SW mode (Wheeler et al. 2000; Kiladis et al. 2009). The theoretical IG0 wave has a cross-equatorial meridional flow with convergence away from the equator and antisymmetric zonal wind pattern (Kiladis et al. 2009). Both in the NH and SH base points, the circulation field associated with enhanced precipitation broadly resembles the IG0 SW mode, with cross-equatorial meridional flow and a low east of the maximum convection and a high west of it. The resemblance of reanalysis-based IG0 wave dynamical fields to its theoretical structure is well documented in the NH and different ocean basins (Wheeler et al. 2000; Kiladis et al. 2009), and thus, it is satisfying to see similar structures in the EP and also for the SH base point. In the regions of suppressed convection, there are pronounced cross-equatorial meridional components of wind feeding into the enhanced convection region in the opposite hemisphere, helping us distinguish IG0 waves (antisymmetric) from Kelvin waves (symmetric) despite there being some spectral filtering overlap (see Fig. 3 of Kiladis et al. 2009).

3) MRG–TD-TYPE DISTURBANCES

The structure of the regressed 850-hPa wind and precipitation anomalies onto MRG–TD-type filtered precipitation anomalies at the NH and SH base point are shown in Fig. 9. Although the percent variance associated with MRG–TD-type filtered band is the largest among all CCWs (Fig. 3), this is inflated due to the large spectral bandwidth. Furthermore, even though the percent variance is largest during FMA, we note that the amplitude of MRG–TD-type precipitation anomalies over the EP from day −1 through day +1 is not as strong as in June–November for TD-type disturbances (Serra et al. 2008). The enhanced and suppressed precipitation centers move westward in both hemispheres at an approximate phase speed of 7–11 m s^{-1} with zonal wavenumber 8–12 and an approximate period of 4–8 days.

On day −1 for the NH base point (Fig. 9a), a statistically significant suppressed convective center is detected at around 115°W as well as an enhanced convection center east of the base point with cross-equatorial southerlies. At each of the three lags, cross-equatorial wind flow is seen in both hemispheres, but the signals are stronger for the NH base point. Gyres in the streamfunction are displaced a bit south of the equator for the NH base point in all three lags. Yokoyama and Takayabu (2012) suggested that the cross-equatorial 850-hPa winds are more significant than in the boundary layer, while the vortex structure is more significant near the surface. However, we do not find statistically significant vorticity anomalies at 1000 hPa (not shown). At subsequent lags, enhanced precipitation moves westward with cross-equatorial southerly inflow.

The horizontal structure of MRG–TD-type band-filtered 850-hPa winds, streamfunction, and precipitation anomalies onto

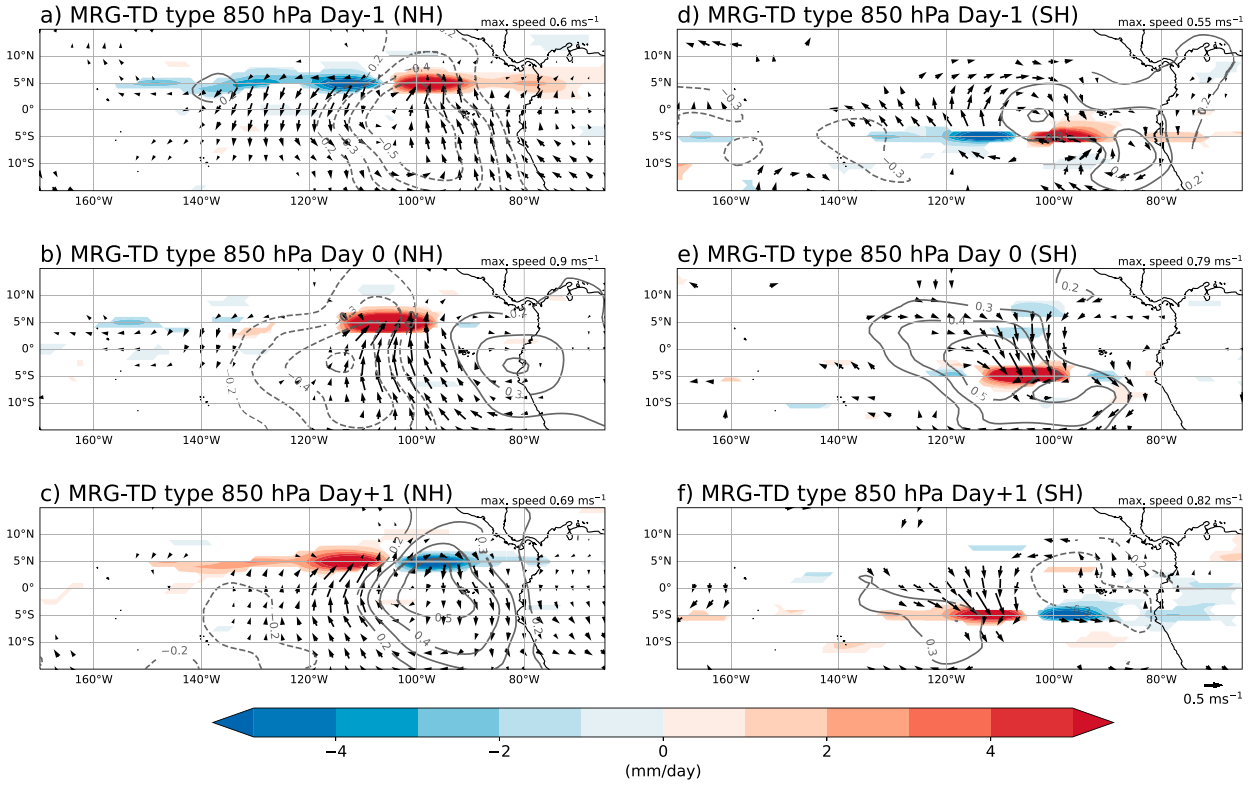

FIG. 9. As in Fig. 6, but for MRG–TD-type wave-band filtered precipitation (shading), streamfunction (contours), and the wind (vectors) anomalies at the base point (a)–(c) 5°N, 105°W and (d)–(f) 5°S, 105°W for day −1, day 0, and day +1 at 850 hPa. Streamfunction contours start at $\pm 5 \times 10^5$ m^2 s^{-1} and are plotted every 10^5 m^2 s^{-1} with negative contours dashed.

MRG–TD-type filtered anomalies for the SH base point show a weaker and less distinctive pattern (Figs. 9d–f). Cross-equatorial circulations are found, but they are not as spatially coherent as they are at the NH base point. At day −1, a very weak enhanced precipitation region is seen at around 95°W with suppressed convection to the west. This enhanced precipitation region moves westward and strengthens with northerly wind convergence at the convection center at day 0. The gyres in the enhanced or suppressed regions are weaker compared to the NH base point. However, there is at least a hint of an antisymmetric precipitation signal for the SH base point. At day +1, the enhanced precipitation signal becomes weaker and is seen at around 115°W. Our SH base-point composite pattern is roughly similar to Frank and Roundy (2006), where they investigated outgoing longwave radiation anomalies and showed MRG–TD-type waves have high variance in the southern Indian and South Pacific Oceans during FMA, but the composite structure is weaker than in it is in the NH during the SH warm season (December–April).

c. *IMERG precipitation-based ITCZ states*

1) DAILY EAST PACIFIC ITCZ STATES

Figure 10 shows a comparison between our new, IMERG precipitation-based and GridSat IR imagery-based ITCZ states (Haffke et al. 2016) for each of the five ITCZ states: nITCZ, sITCZ, aITCZ, dITCZ, and eITCZ. The results are robust to the precipitation dataset as we also have seen consistent patterns and ITCZ-state percentages with 2001–21 daily precipitation data from NCEP's Climate Forecast System Reanalysis (CFSR; Saha et al. 2006, 2014) versions 1 and 2, NASA's Modern-Era Retrospective Analysis for Research and Applications, version 2 (MERRA-2; Gelaro et al. 2017), and ERA5 (not shown).

We see general agreement in the spatial pattern and ITCZ-state percentages for our new IMERG precipitation-based ITCZ states with the Haffke et al. (2016) GridSat IR satellite imagery ITCZ states. Figure 10 shows that the time mean precipitation structures are similar, with the exception of eITCZs and to a greater extent aITCZs. Our new IMERG ITCZ states algorithm has substantially more nITCZs (60.2%) and sITCZs (14.6%) and fewer dITCZs (13.2%) compared to the GridSat IR imagery-based ITCZ states. Another feature that is not captured in the GridSat IR imagery-based ITCZ states is that our new algorithm has a latitudinally confined double-ITCZ-like structure for the eITCZ state. We caution a direct comparison of the eITCZ structure, however, as there were only two eITCZ days for the 2001–12 overlapping timeframe of IMERG data and GridSat IR ITCZ states. Subsequent analyses of the eITCZ state suggest that an on-equatorial precipitation maxima requires strong EP El Niño years (i.e., 1982/83, 1997/98). Detailed comparisons between daily precipitation-based ITCZ states in observations and reanalyses are being conducted in a separate study.

As discussed in section 2, we anticipated differences in the structure and occurrence of the aITCZ state. Note that there are

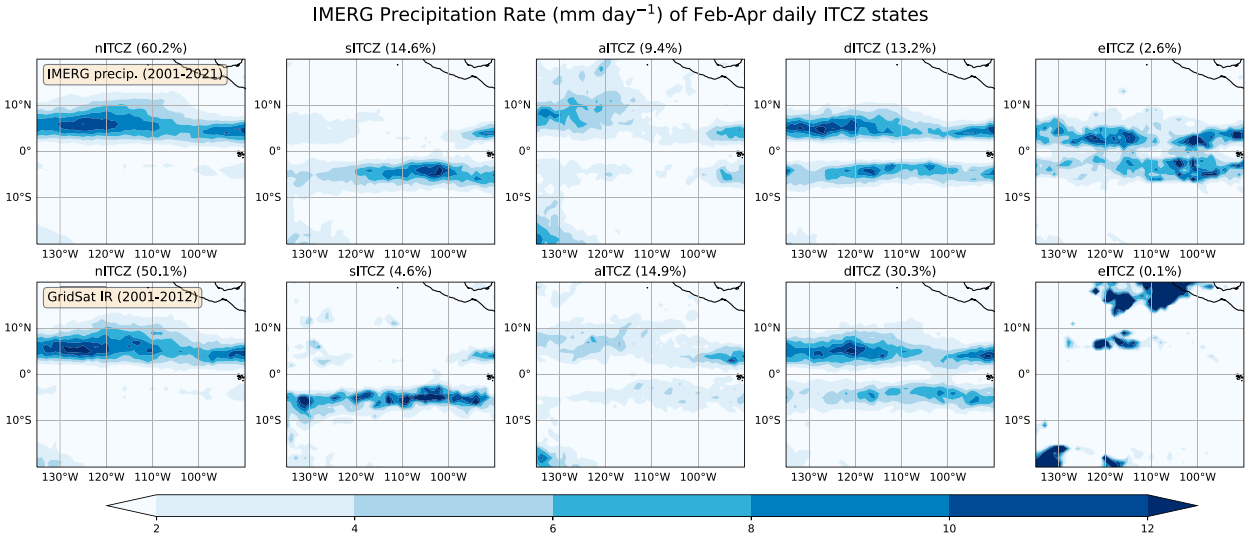

FIG. 10. FMA average IMERG precipitation rate (mm day^{-1}) composited for each daily EP ITCZ state: northern (nITCZ), southern (sITCZ), absent (aITCZ), double (dITCZ), and equatorial (eITCZ) using (top) the IMERG precipitation-based algorithm (2001–21) and (bottom) GridSat IR imagery-based algorithm (2001–12).

consistent ITCZ/CCW results between our new precipitation-based ITCZ states and the GridSat IR imagery-based ITCZ states, but the time period is much shorter (12 years rather than 21 years; not shown) when analyzing the GridSat IR ITCZ states.

Figure 11 shows the temporal distribution of our new IMERG daily ITCZ states for FMA from 2001 to 2021. There is a loose seasonality to most ITCZ states, with nITCZs occurring at the beginning and end of the three months, aITCZs occurring at the beginning of the 3 months, dITCZs and sITCZs occurring in the middle of the three months, and eITCZs more randomly distributed. In addition, there is strong interannual variability in ITCZ states, with some years comprising mostly nITCZs and while other years contain more instances of dITCZs and sITCZs (not shown). We also note that eITCZs occur only for some years, possibly associated with whether an equatorial cold tongue is present and the strength or flavor of ENSO (Yang and Magnusdottir 2016). Detailed analyses of interannual variability are left for a future study.

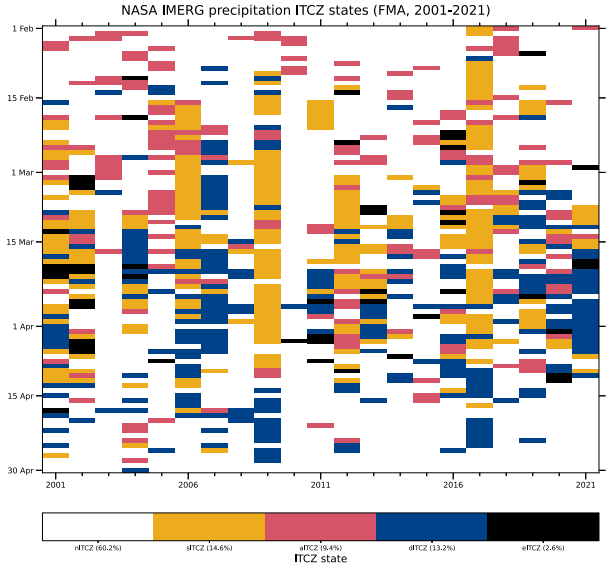

FIG. 11. FMA 2001–21 temporal variability of daily EP ITCZ states using the IMERG precipitation-based algorithm.

2) CCW VARIABILITY AS A FUNCTION OF ITCZ STATES

To further analyze the relative CCW influence on the ITCZ over the EP during boreal spring, we examine how the CCW-filtered percent precipitation variance differs for each ITCZ state. To do this, we repeat the process of calculating the percent variance for each filtered CCW over the EP (10°S–10°N, 75°–135°W) but limit the composites to the subset of days during our FMA season associated with each ITCZ state.

Figure 12a shows that for each one of the six waves, the filtered CCW contribution to the precipitation variance is far less for nITCZ days than it is for all FMA days. For the cumulative impact of filtered CCWs on precipitation variance for each ITCZ state (Fig. 12b), the CCW contribution to the precipitation gradually increases from nITCZ (55.3%) to dITCZ (79.3%) with additional variance explained for sITCZ (105.9%) and eITCZ (121.5%) states. It is important to note that these fractional variances are overestimates of the true variance and are strongly dependent on the size and location of each filter box. The values higher than 100% represent a greater degree of variability and this occurs when the standard deviation exceeds the mean value of the dataset. The most dominant influence of CCWs on the precipitation variance occurs during sITCZ and eITCZ days, and it is most prominent for the three leading high-frequency CCW bands of Kelvin, IG0, and MRG–TD-type waves. Even though the

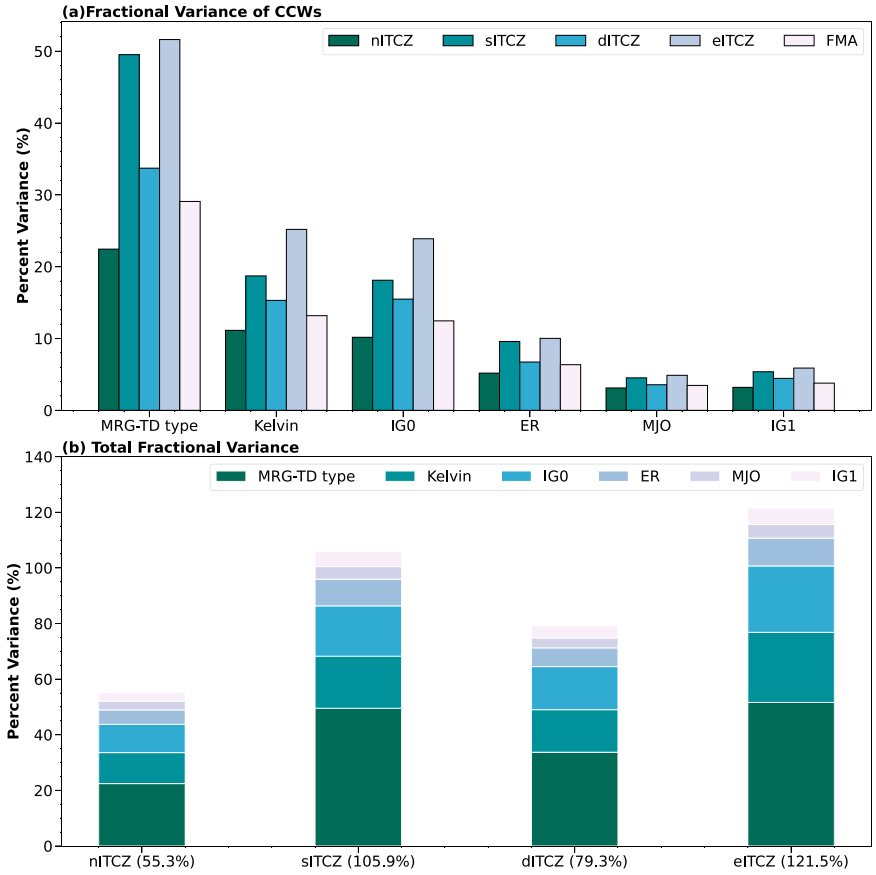

FIG. 12. (a) Averaged percent variance of each ITCZ state explained by wave-filtered FMA precipitation variance from the following wave bands: MRG–TD type, Kelvin, IG0, ER, MJO, and IG1. The fifth bar is for the averaged percent variance of total precipitation explained by each wave type. (b) Total variance of wave-filtered precipitation expressed as a fraction of the ITCZ-state variance for all CCW bands. The variance has been calculated from 2001 through 2021 and averaged within 10°N–10°S, 75°–135°W. We withhold aITCZ variances since there is less precipitation activity associated with this state.

nITCZ state is the most dominant state throughout the year, CCW-filtered precipitation activity has a relatively small contribution to the total precipitation variability (Fig. 12) when only the northern branch of ITCZ is active. On the other hand, the relative contribution of CCW peaks when there is precipitation activity near the equator or in the SH (Fig. 12b), which is in broad agreement with the percent variance maps shown in Fig. 4.

These results are likely due to the standard deviation of total anomalous precipitation being larger in the NH than near the equator and in the SH. In the standardization process, the larger values do not dominate the lower values by making the standardized anomaly smaller. Nonetheless, these strong contributions by filtered CCWs suggest that they are highly correlated with SH precipitation since, except for the nITCZ state, all other ITCZ states have precipitation activity in SH (Fig. 10). Interestingly, the eITCZ percent variance exceeds that of sITCZ for each of the filter wave band. The eITCZ state from the GridSat IR algorithm has been shown to be frequent only for El Niño years when the EP cold tongue is replaced by warmer SSTs (Haffke et al. 2016). Furthermore, Yang and Magnusdottir (2016) showed during dITCZ and sITCZ days that the SST anomalies are warmer south of the equator over the EP. These results altogether suggest that interannual variability (i.e., warmer background SSTs) may play a substantial role in increased CCW precipitation activity near and south of the equator over the EP.

3) COEVOLUTION BETWEEN ITCZ STATES AND LEADING HIGH-FREQUENCY CCWS

Finally, we examine the coevolution between ITCZ states and the three leading high-frequency CCWs to determine if there is a significant lead–lag relationship. We analyze only strongly precipitating CCW days, which are defined as the subset of FMA days when CCW precipitation anomalies exceed 1.0 standard deviation at the base point (NH or SH). These strong CCW days are averaged in time and considered as lag 0 for each respective CCW. We then quantify the time lag, from −15 to +15 days, as a function of longitude by

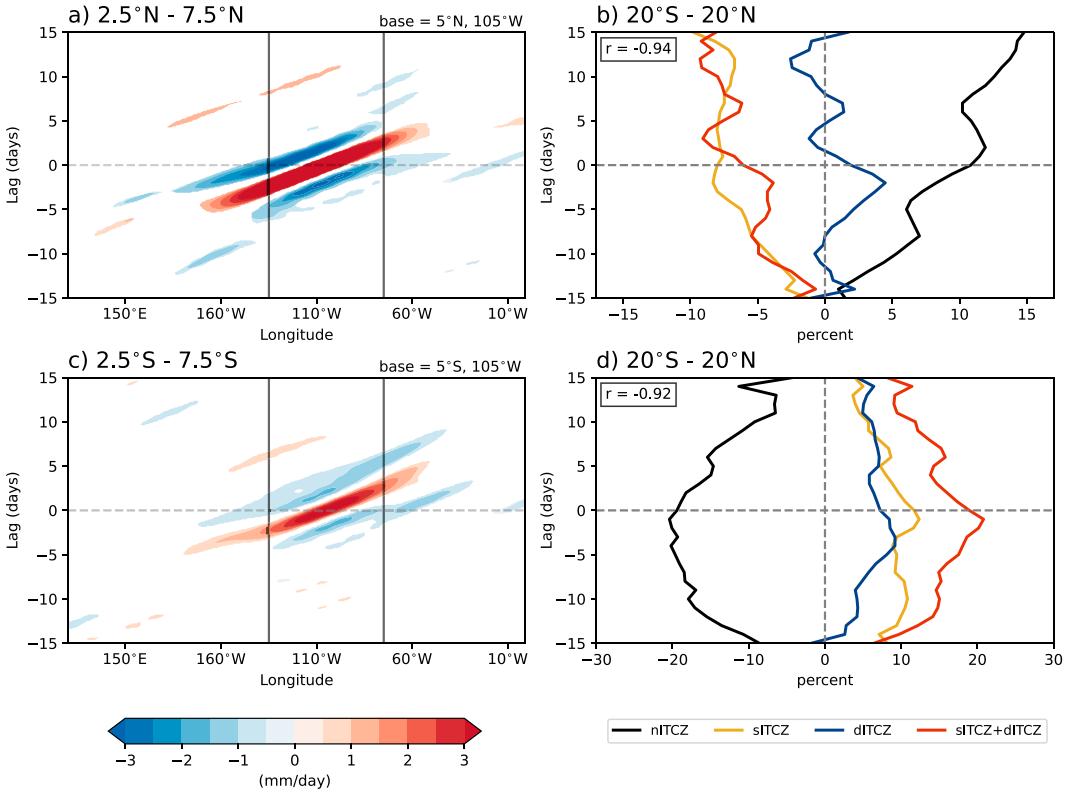

FIG. 13. Longitude–time diagram of Kelvin wave-band filtered precipitation anomalies averaged between (a) 2.5°–7.5°N and (c) 2.5°–7.5°S. Lag 0 corresponds to the days when the Kelvin wave-filtered precipitation anomalies are greater than one standard deviation at the NH and SH base points shown in the top-right corners. The black vertical lines enclose the ITCZ-state longitude window. The anomalies shown here are 99% significant by a two-sided Student's *t* test. (b),(d) ITCZ-state percent anomalies for strong Kelvin wave-band activity days for the NH and SH base points, respectively. Lag 0 is as in (a) and (c). The *r* value at the top left shows the correlation between nITCZ and sITCZ + dITCZ.

computing the latitudinal average of the precipitation anomalies over 2.5°–7.5°N (NH) and 2.5°–7.5°S (SH).

To relate the leading high-frequency CCW precipitation activity with the ITCZ state, we start by calculating the ITCZ-state percentage for strong wave activity days for lag −15 to +15, where lag 0 for each CCW type is the same as described above. The ITCZ-state percentage is plotted as anomalies that are relative to the FMA percentages in Fig. 10 after applying a 5-day running mean to the percentage anomalies.

Kelvin waves initiate in the central–west Pacific near day −5 and propagate into the EP (Figs. 13a,c) whereas the IG0 waves (Figs. 14a,c) and MRG–TD-type waves (Figs. 15a,c) are mostly confined to the EP. For all three CCWs, the precipitation signals in the SH are much weaker than in the NH, which is expected based on climatological precipitation variances for each CCW (not shown). The pattern of strong Kelvin wave variances over the entire Pacific basin agrees with past studies (Straub and Kiladis 2002; Roundy and Frank 2004). IG0 waves show significant precipitation signals in the central Pacific (Figs. 14a,c), but they are not as coherent as those of Kelvin waves. MRG–TD-type waves originate and dissipate within the EP (Figs. 15a,c) unlike summertime when a significant portion of these waves can originate over western Africa and the Atlantic Ocean basin (Serra et al. 2008, their Fig. 6).

In regard to the time evolution of ITCZ states for NH CCWs, there is a broadly increasing trend for nITCZs (black curves) and decreasing trend for sITCZs (gold curves) while dITCZs (blue curves) decrease after lag 0 (Figs. 13b, 14b, and 15b). Together, the sITCZ and dITCZ trend (sITCZ + dITCZ; red curves) is strongly anticorrelated with nITCZs ($r \leq -0.92$). The increasing frequency of the nITCZ state, particularly after lag 0, suggests that NH CCWs may act as a precursor and aid in the development of the nITCZ state.

For SH CCWs (Figs. 13d, 14d, and 15d), the ITCZ-state percent anomalies are nearly double (as high as ≈25%) the NH CCWs ITCZ-state percent anomalies (note the different abscissa). This is significant in that a 25% increase in sITCZ and dITCZ together would bring their total percentage to above 50% and nITCZs would fall below 40%. The sITCZs have the largest percentage increase, and nITCZ has the largest percentage decrease, both reaching their largest deviations near lag 0. The dITCZs show relatively smaller percent anomalies but have a somewhat more identifiable temporal peak

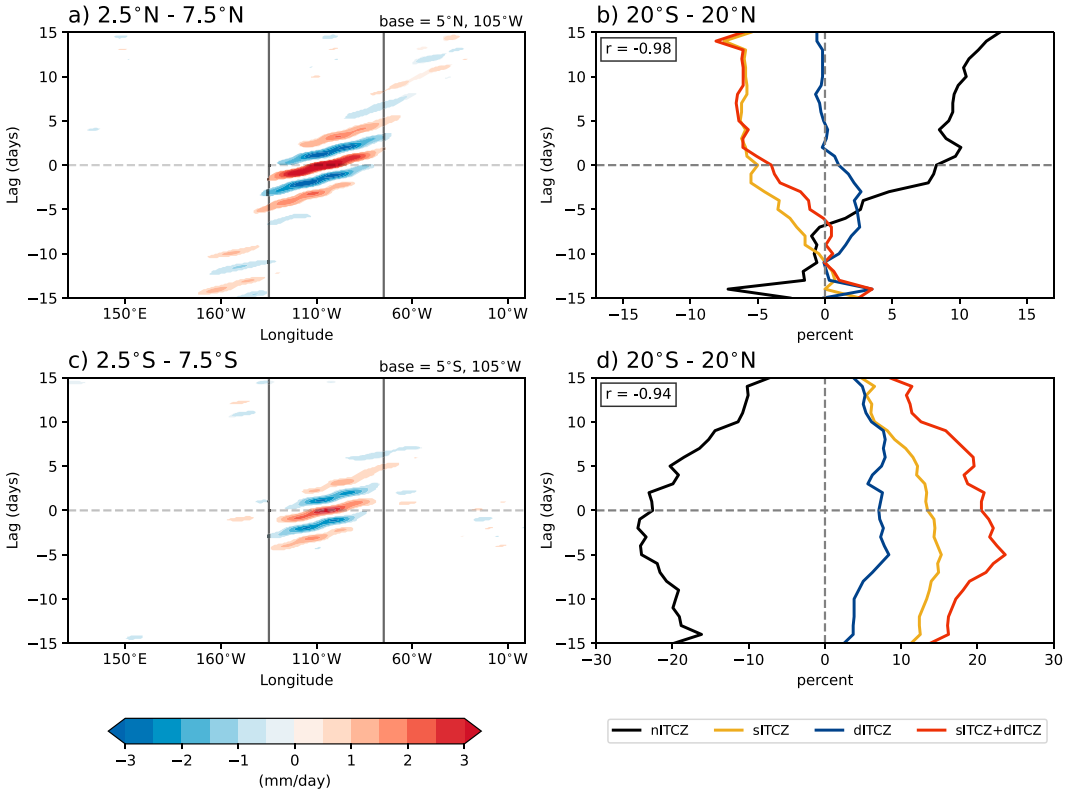

FIG. 14. As in Fig. 13, but for the IG0 wave band.

near lag 0 than sITCZs. Similar to that of NH CCWs, the sITCZ + dITCZ trend is highly anticorrelated with the nITCZ trend ($r \leq -0.87$). These results imply that SH CCWs can both aid in the development of sITCZs or dITCZs (i.e., positive ITCZ anomalies at positive lags) and be excited/amplified by sITCZs or dITCZs (i.e., increasing ITCZ-state trends at negative lags that proceed CCWs). This generally agrees with the Hovmöller diagrams in Figs. 13–15 in that all CCWs are more narrowly confined to the EP for the SH base point compared to the NH base point.

4. Summary and conclusions

In this study, we demonstrated that there is a significant impact of filtered CCWs on precipitation variability over the EP during boreal spring, the only season with significant precipitation activity in the SH, using IMERG precipitation and ERA5 reanalysis data. We employed commonly used space–time filtering techniques (Wheeler and Kiladis 1999; Dias and Kiladis 2014, and many others). We computed the percent precipitation variance contributed by each of six CCW band filtered precipitation (Kelvin, IG0, MRG-TD-type, ER, MJO, and IG1) following the methods of Schreck et al. (2013) with respect to (i) all FMA days and (ii) days associated with each of five different ITCZ configurations or "ITCZ states" (nITCZ, sITCZ, aITCZ, dITCZ, and eITCZ) based on our new daily precipitation-based ITCZ-state algorithm.

The results show that the percent of CCW-filtered precipitation variances have a synchronized seasonal cycle of maximum variance explained during FMA and minimum variance explained during ASO or NDJ over the EP. Furthermore, the impact is more predominant with higher precipitation variance explained by filtered CCWs bands in the SH (0°–15°S) than in the NH (15°N–0°). Our analysis shows that there are three leading high-frequency CCWs (Kelvin, IG0, and MRG–TD type) over the EP, especially during FMA (Fig. 3). At the same time, caution must be taken comparing percentages between wave bands as the background variance inflates larger spectral widths, especially for the wide spectral band of MRG–TD type.

We examined the composite time-evolving dynamical patterns of the three leading high-frequency CCWs (Kelvin, IG0, and MRG–TD type) at both NH and SH base points during FMA with a lag-linear regression technique. The lower tropospheric dynamical fields of the Kelvin and IG0 waves at both base points broadly resemble the theoretically predicted modes from equatorial wave theory (Blandford 1966; Matsuno 1966; Wheeler et al. 2000; Kiladis et al. 2009). The Kelvin wave precipitation anomalies and dynamical fields at both base points show a relatively slow eastward propagation of 17–18 m s^{-1} and a large spatial scale (zonal wavenumber 6–7). In contrast to the Indo-Pacific warm pool, we find a meridionally narrow and zonally elongated Kelvin wave precipitation band along with a weak but significant amount of lower tropospheric meridional wind component close to the maximum precipitation. At the NH base point, the Kelvin wave precipitation is north of the

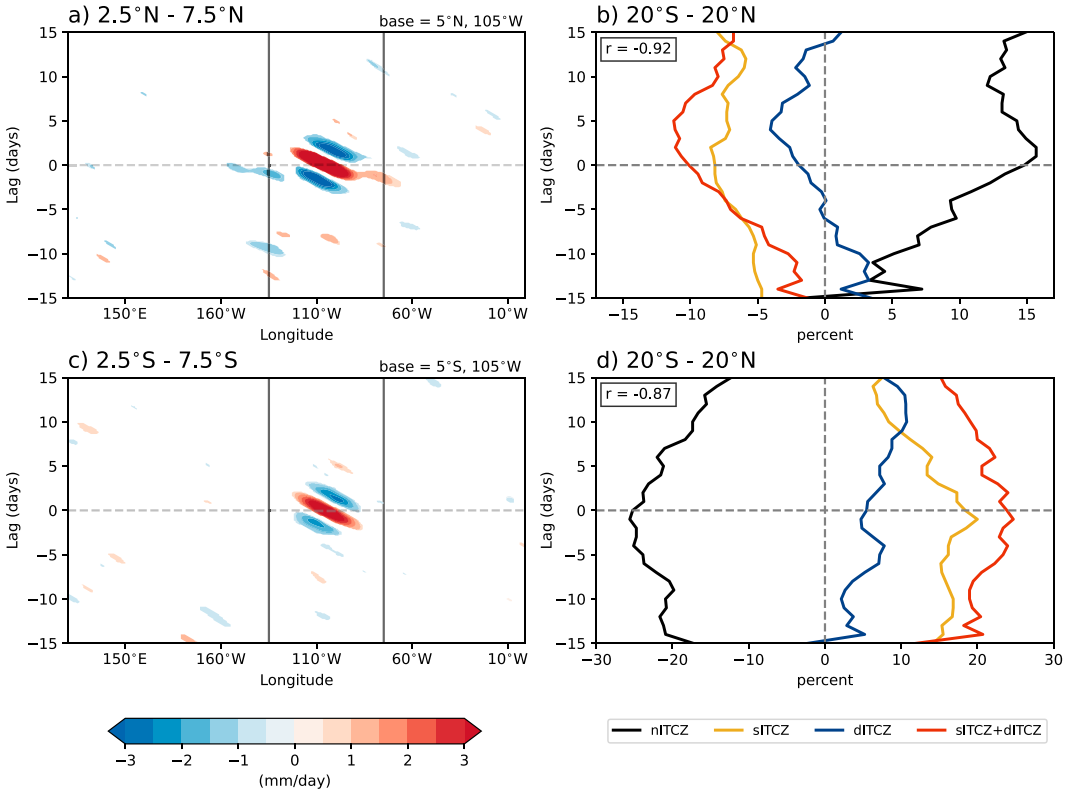

FIG. 15. As in Fig. 13, but for the MRG–TD-type wave band.

equator; however, in the SH, the precipitation anomalies are more like a double-ITCZ pattern (Figs. 6 and 7). These precipitation patterns in both hemispheres suggest that the anomalies follow the boreal spring background SST pattern (Straub and Kiladis 2002; Kiladis et al. 2009). Despite the fact that Kelvin waves and IG0 have some spectral overlap, we see characteristics that distinguish the two consistent with equatorial wave theory.

IG0 waves are of slightly smaller spatial scales (zonal wavenumber 8) and have faster eastward propagation speeds (22–23 m s^{-1}). IG0 waves are dominated by strong cross-equatorial meridional flow with minimal zonal flow except that associated with zonal wind convergence into the enhanced precipitation (Fig. 8). Furthermore, IG0 waves have more of an SH-only precipitation anomaly for the SH base point compared to more of a double-ITCZ anomalous precipitation structure for Kelvin waves. Last, Kelvin waves have a robust upper-level dynamical signal, which is entirely absent from IG0 waves.

Unlike other studies on the EP easterly waves (Serra et al. 2008; Huaman et al. 2021), the westward-propagating MRG–TD-type wave band shows unique composite precipitation and dynamical patterns during boreal spring. The MRG–TD-type wave band shows convective propagation speeds of 7–11 m s^{-1} and relatively small zonal wavenumbers of 8–12. Even though our results show that the relative impact of the MRG–TD-type filtered wave band on precipitation variance is strong during FMA (Fig. 3), we find that the composite dynamical structure is not as coherent as that of Kelvin or IG0 waves, and the precipitation anomalies do not propagate as far (Fig. 9). This is somewhat expected, considering that tropical cyclogenesis is uncommon over the EP during boreal spring.

Our analysis suggests that the filtered CCW bands have a stronger impact on the EP ITCZ when precipitation occurs in the SH (i.e., dITCZ, sITCZ, and eITCZ states). The results show that the CCW filtered variances are much higher during the sITCZ and eITCZ days for all CCWs (Fig. 12). However, the eITCZ state is a rare phenomenon and is mostly active during EP El Niño years (Haffke et al. 2016).

Finally, we investigated the coevolution of the precipitation associated with the three leading high-frequency CCWs and ITCZ states. The Kelvin wave convective signal can be seen propagating from the central–west Pacific and IG0 and MRG–TD type are only localized in the EP (Figs. 13–15). We find consistency for the CCW–ITCZ-state relationship at the NH base point for all three leading high-frequency CCWs. The nITCZ percentage increases strongly after lag 0 while the sITCZ and dITCZ together have an overall decreasing trend, which suggests increased CCW activity may facilitate the more frequent nITCZ activity. However, at the SH base point, we show that the sITCZ and dITCZ (combined) percentage increase and nITCZ percentage decrease are largest at lag 0, suggesting CCWs may excite the sITCZ- or dITCZ-state activity or sITCZs/dITCZs can excite CCWs in the SH.

In this study, we document that although precipitation activity is present in the NH throughout the year, variability in the precipitation is high in a fractional sense during boreal

spring and CCWs strongly influence precipitation, especially in the SH. To our knowledge, this is the first study to investigate the impacts of CCWs on precipitation variability over the EP during boreal spring in a fractional sense. However, further investigation of the detailed mechanisms is needed to understand the interactions between the background state, the ITCZ state, and CCW activity over the EP during boreal spring when the SH ITCZ is present. Given that Earth system models struggle to capture the correct seasonality, structure, and life cycle of both CCWs and the ITCZ, future work will involve identifying CCW–ITCZ relationships in Earth system models and determining which, if any, Earth system models faithfully reproduce the observed CCW and ITCZ variability in the EP.

Acknowledgments. We would like to acknowledge insightful conversations with Gudrun Magnusdottir. We thank Carl Schreck for his methodology for calculating the percent variances of CCWs. Commments from George Kiladis and two anonymous reviewers helped improve the quality of the final manuscript. Financial support comes from NSF Grant AGS-1953944 and NSF Grant AGS-2303225.

Data availability statement. IMERG data were accessed from the NASA Goddard Earth Sciences (GES) Data and Information Services Center (DISC) and are available at https://disc.gsfc.nasa.gov/datasets/GPM_3IMERGDF_06/summary. The ERA5 surface data can be downloaded from https://cds.climate.copernicus.eu/cdsapp#!/dataset/reanalysis-era5-pressure-levels. The daily precipitation-based ITCZ-state algorithm data can be downloaded from https://drive.google.com/file/d/11Q5_95M3w_qB4FOJrlAPJM0v3VF8slhp/view?usp=sharing. All scripts used to produce figures for this paper are online via Zenodo (Fahrin 2024).

REFERENCES

Adam, O., T. Schneider, F. Brient, and T. Bischoff, 2016: Relation of the double-ITCZ bias to the atmospheric energy budget in climate models. *Geophys. Res. Lett.*, **43**, 7670–7677, https://doi.org/10.1002/2016GL069465.

Bain, C. L., G. Magnusdottir, P. Smyth, and H. Stern, 2010: Diurnal cycle of the intertropical convergence zone in the East Pacific. *J. Geophys. Res.*, **115**, D23116, https://doi.org/10.1029/2010JD014835.

——, J. D. Paz, J. Kramer, G. Magnusdottir, P. Smyth, H. Stern, and C.-c Wang, 2011: Detecting the ITCZ in instantaneous satellite data using spatiotemporal statistical modeling: ITCZ climatology in the east Pacific. *J. Climate*, **24**, 216–230, https://doi.org/10.1175/2010JCLI3716.1.

Bartana, H., C. Garfinkel, O. Shamir, and J. Rao, 2022: Projected future changes in equatorial wave spectrum in CMIP6. *Climate Dyn.*, **60**, 3277–3289, https://doi.org/10.1007/s00382-022-06510-y.

Berry, G., and M. J. Reeder, 2014: Objective identification of the intertropical convergence zone: Climatology and trends from the ERA-Interim. *J. Climate*, **27**, 1894–1909, https://doi.org/10.1175/JCLI-D-13-00339.1.

Blandford, R., 1966: Mixed gravity-Rossby waves in the ocean. *Deep-Sea Res. Oceanogr. Abstr.*, **13**, 941–961, https://doi.org/10.1016/0011-7471(76)90912-8.

Byrne, M. P., A. G. Pendergrass, A. D. Rapp, and K. R. Wodzicki, 2018: Response of the intertropical convergence zone to climate change: Location, width, and strength. *Curr. Climate Change Rep.*, **4**, 355–370, https://doi.org/10.1007/s40641-018-0110-5.

Chao, W. C., 2007: Chimeric equatorial waves as a better descriptor for "convectively-coupled equatorial waves". *J. Meteor. Soc. Japan*, **85**, 521–524, https://doi.org/10.2151/jmsj.85.521.

Cheng, Y.-M., S. Tulich, G. N. Kiladis, and J. Dias, 2022: Two extratropical pathways to forcing tropical convective disturbances. *J. Climate*, **35**, 6587–6609, https://doi.org/10.1175/JCLI-D-22-0171.1.

Dias, J., and G. N. Kiladis, 2014: Influence of the basic state zonal flow on convectively coupled equatorial waves. *Geophys. Res. Lett.*, **41**, 6904–6913, https://doi.org/10.1002/2014GL061476.

Fahrin, F., 2024: Convectively coupled waves and east Pacific ITCZ relation (v1.1.1). Zenodo, last accessed 7 March 2024, https://doi.org/10.5281/zenodo.10794655.

Ferreira, R. N., and W. H. Schubert, 1997: Barotropic aspects of ITCZ breakdown. *J. Atmos. Sci.*, **54**, 261–285, https://doi.org/10.1175/1520-0469(1997)054<0261:BAOIB>2.0.CO;2.

Frank, W. M., and P. E. Roundy, 2006: The role of tropical waves in tropical cyclogenesis. *Mon. Wea. Rev.*, **134**, 2397–2417, https://doi.org/10.1175/MWR3204.1.

Gelaro, R., and Coauthors, 2017: The Modern-Era Retrospective Analysis for Research and Applications, version 2 (MERRA-2). *J. Climate*, **30**, 5419–5454, https://doi.org/10.1175/JCLI-D-16-0758.1.

Gill, A. E., 1980: Some simple solutions for heat-induced tropical circulation. *Quart. J. Roy. Meteor. Soc.*, **106**, 447–462, https://doi.org/10.1002/qj.49710644905.

Gonzalez, A. O., I. Ganguly, M. C. McGraw, and J. G. Larson, 2022: Rapid dynamical evolution of ITCZ events over the East Pacific. *J. Climate*, **35**, 1197–1213, https://doi.org/10.1175/JCLI-D-21-0216.1.

Gu, G., R. F. Adler, and A. H. Sobel, 2005: The eastern Pacific ITCZ during the boreal spring. *J. Atmos. Sci.*, **62**, 1157–1174, https://doi.org/10.1175/JAS3402.1.

Guo, Y., D. E. Waliser, and X. Jiang, 2015: A systematic relationship between the representations of convectively coupled equatorial wave activity and the Madden–Julian oscillation in climate model simulations. *J. Climate*, **28**, 1881–1904, https://doi.org/10.1175/JCLI-D-14-00485.1.

Haffke, C., G. Magnusdottir, D. Henke, P. Smyth, and Y. Peings, 2016: Daily states of the March–April East Pacific ITCZ in three decades of high-resolution satellite data. *J. Climate*, **29**, 2981–2995, https://doi.org/10.1175/JCLI-D-15-0224.1.

Heath, A., A. O. Gonzalez, M. Gehne, and A. Jaramillo, 2021: Interactions of large-scale dynamics and Madden-Julian oscillation propagation in multi-model simulations. *J. Geophys. Res. Atmos.*, **126**, e2020JD033988, https://doi.org/10.1029/2020JD033988.

Hendon, H. H., and B. Liebmann, 1991: The structure and annual variation of antisymmetric fluctuations of tropical convection and their association with Rossby–gravity waves. *J. Atmos. Sci.*, **48**, 2127–2140, https://doi.org/10.1175/1520-0469(1991)048<2127:TSAAVO>2.0.CO;2.

Henke, D., P. Smyth, C. Haffke, and G. Magnusdottir, 2012: Automated analysis of the temporal behavior of the double intertropical convergence zone over the East Pacific. *Remote Sens. Environ.*, **123**, 418–433, https://doi.org/10.1016/j.rse.2012.03.022.

Hersbach, H., and Coauthors, 2020: The ERA5 global reanalysis. *Quart. J. Roy. Meteor. Soc.*, **146**, 1999–2049, https://doi.org/10.1002/qj.3803.

Hollis, M. A., R. R. McCrary, J. P. Stachnik, C. Lewis-Merritt, and E. R. Martin, 2023: A global climatology of tropical easterly waves. *Climate Dyn.*, https://doi.org/10.1007/s00382-023-07025-w, in press.

Horinouchi, T., 2013: Modulation of seasonal precipitation over the tropical western/central Pacific by convectively coupled mixed Rossby–gravity waves. *J. Atmos. Sci.*, **70**, 600–606, https://doi.org/10.1175/JAS-D-12-0283.1.

Huaman, L., and K. Takahashi, 2016: The vertical structure of the eastern Pacific ITCZS and associated circulation using the TRMM Precipitation Radar and in situ data. *Geophys. Res. Lett.*, **43**, 8230–8239, https://doi.org/10.1002/2016GL068835.

——, and C. Schumacher, 2018: Assessing the vertical latent heating structure of the East Pacific ITCZ using the *CloudSat* CPR and TRMM PR. *J. Climate*, **31**, 2563–2577, https://doi.org/10.1175/JCLI-D-17-0590.1.

——, ——, and G. N. Kiladis, 2020: Eastward-propagating disturbances in the tropical Pacific. *Mon. Wea. Rev.*, **148**, 3713–3728, https://doi.org/10.1175/MWR-D-20-0029.1.

——, E. D. Maloney, C. Schumacher, and G. N. Kiladis, 2021: Easterly waves in the East Pacific during the OTREC 2019 field campaign. *J. Atmos. Sci.*, **78**, 4071–4088, https://doi.org/10.1175/JAS-D-21-0128.1.

Huang, P., and R. Huang, 2011: Climatology and interannual variability of convectively coupled equatorial waves activity. *J. Climate*, **24**, 4451–4465, https://doi.org/10.1175/2011JCLI4021.1.

Hubert, L. F., A. F. Krueger, and J. S. Winston, 1969: The double intertropical convergence zone—Fact or fiction? *J. Atmos. Sci.*, **26**, 771–773, https://doi.org/10.1175/1520-0469(1969)026<0771:TDICZF>2.0.CO;2.

Huffman, G. J., D. T. Bolvin, D. Braithwaite, K. Hsu, R. Joyce, P. Xie, and S.-H. Yoo, 2015: NASA Global Precipitation Measurement (GPM) Integrated Multi-satellitE Retrievals for GPM (IMERG). Algorithm Theoretical Basis Doc., version 4, 26 pp., https://doi.org/10.1007/978-3-030-24568-9_19.

Hung, M.-P., J.-L. Lin, W. Wang, D. Kim, T. Shinoda, and S. J. Weaver, 2013: MJO and convectively coupled equatorial waves simulated by CMIP5 climate models. *J. Climate*, **26**, 6185–6214, https://doi.org/10.1175/JCLI-D-12-00541.1.

Hwang, Y.-T., and D. M. W. Frierson, 2013: Link between the double-intertropical convergence zone problem and cloud biases over the Southern Ocean. *Proc. Natl. Acad. Sci. USA*, **110**, 4935–4940, https://doi.org/10.1073/pnas.1213302110.

Judt, F., and R. Rios-Berrios, 2021: Resolved convection improves the representation of equatorial waves and tropical rainfall variability in a global nonhydrostatic model. *Geophys. Res. Lett.*, **48**, e2021GL093265, https://doi.org/10.1029/2021GL093265.

Kiladis, G. N., 1998: Observations of Rossby waves linked to convection over the eastern tropical Pacific. *J. Atmos. Sci.*, **55**, 321–339, https://doi.org/10.1175/1520-0469(1998)055<0321:OORWLT>2.0.CO;2.

——, M. C. Wheeler, P. T. Haertel, K. H. Straub, and P. E. Roundy, 2009: Convectively coupled equatorial waves. *Rev. Geophys.*, **47**, RG2003, https://doi.org/10.1029/2008RG000266.

——, J. Dias, and M. Gehne, 2016: The relationship between equatorial mixed Rossby–gravity and eastward inertio-gravity waves. Part I. *J. Atmos. Sci.*, **73**, 2123–2145, https://doi.org/10.1175/JAS-D-15-0230.1.

Kim, J.-E., and M. J. Alexander, 2013: Tropical precipitation variability and convectively coupled equatorial waves on submonthly time scales in reanalyses and TRMM. *J. Climate*, **26**, 3013–3030, https://doi.org/10.1175/JCLI-D-12-00353.1.

Knutson, T. R., and K. M. Weickmann, 1987: 30–60 day atmospheric oscillations: Composite life cycles of convection and circulation anomalies. *Mon. Wea. Rev.*, **115**, 1407–1436, https://doi.org/10.1175/1520-0493(1987)115<1407:DAOCLC>2.0.CO;2.

Liebmann, B., G. N. Kiladis, L. M. V. Carvalho, C. Jones, C. S. Vera, I. Bladé, and D. Allured, 2009: Origin of convectively coupled Kelvin waves over South America. *J. Climate*, **22**, 300–315, https://doi.org/10.1175/2008JCLI2340.1.

Lin, J.-L., 2007: The double-ITCZ problem in IPCC AR4 coupled GCMS: Ocean–atmosphere feedback analysis. *J. Climate*, **20**, 4497–4525, https://doi.org/10.1175/JCLI4272.1.

——, and Coauthors, 2006: Tropical intraseasonal variability in 14 IPCC AR4 climate models. Part I: Convective signals. *J. Climate*, **19**, 2665–2690, https://doi.org/10.1175/JCLI3735.1.

Lubis, S. W., and C. Jacobi, 2015: The modulating influence of convectively coupled equatorial waves (CCEWS) on the variability of tropical precipitation. *Int. J. Climatol.*, **35**, 1465–1483, https://doi.org/10.1002/joc.4069.

Madden, R. A., and P. R. Julian, 1971: Detection of a 40–50 day oscillation in the zonal wind in the tropical Pacific. *J. Atmos. Sci.*, **28**, 702–708, https://doi.org/10.1175/1520-0469(1971)028<0702:DOADOI>2.0.CO;2.

——, and ——, 1972: Description of global-scale circulation cells in the tropics with a 40–50 day period. *J. Atmos. Sci.*, **29**, 1109–1123, https://doi.org/10.1175/1520-0469(1972)029<1109:DOGSCC>2.0.CO;2.

Maloney, E. D., and J. T. Kiehl, 2002: MJO-related SST variations over the tropical eastern Pacific during Northern Hemisphere summer. *J. Climate*, **15**, 675–689, https://doi.org/10.1175/1520-0442(2002)015<0675:MRSVOT>2.0.CO;2.

Mapes, B. E., T. T. Warner, and M. Xu, 2003: Diurnal patterns of rainfall in northwestern South America. Part III: Diurnal gravity waves and nocturnal convection offshore. *Mon. Wea. Rev.*, **131**, 830–844, https://doi.org/10.1175/1520-0493(2003)131<0830:DPORIN>2.0.CO;2.

Masunaga, H., 2007: Seasonality and regionality of the Madden–Julian oscillation, Kelvin wave, and equatorial Rossby wave. *J. Atmos. Sci.*, **64**, 4400–4416, https://doi.org/10.1175/2007JAS2179.1.

Matsuno, T., 1966: Quasi-geostrophic motions in the equatorial area. *J. Meteor. Soc. Japan*, **44**, 25–43, https://doi.org/10.2151/jmsj1965.44.1_25.

Matthews, A. J., 2000: Propagation mechanisms for the Madden-Julian oscillation. *Quart. J. Roy. Meteor. Soc.*, **126**, 2637–2651, https://doi.org/10.1002/qj.49712656902.

Mayta, V. C., G. N. Kiladis, J. Dias, P. L. S. Dias, and M. Gehne, 2021: Convectively coupled Kelvin waves over tropical South America. *J. Climate*, **34**, 6531–6547, https://doi.org/10.1175/JCLI-D-20-0662.1.

Mechoso, C. R., and Coauthors, 1995: The seasonal cycle over the tropical Pacific in coupled ocean–atmosphere general circulation models. *Mon. Wea. Rev.*, **123**, 2825–2838, https://doi.org/10.1175/1520-0493(1995)123<2825:TSCOTT>2.0.CO;2.

Raymond, D. J., G. B. Raga, C. S. Bretherton, J. Molinari, C. López-Carrillo, and Ž. Fuchs, 2003: Convective forcing in the intertropical convergence zone of the eastern Pacific. *J. Atmos. Sci.*, **60**, 2064–2082, https://doi.org/10.1175/1520-0469(2003)060<2064:CFITIC>2.0.CO;2.

Roundy, P. E., 2020: Interpretation of the spectrum of eastward-moving tropical convective anomalies. *Quart. J. Roy. Meteor. Soc.*, **146**, 795–806, https://doi.org/10.1002/qj.3709.

——, and W. M. Frank, 2004: A climatology of waves in the equatorial region. *J. Atmos. Sci.*, **61**, 2105–2132, https://doi.org/10.1175/1520-0469(2004)061<2105:ACOWIT>2.0.CO;2.

Saha, S., and Coauthors, 2006: The NCEP Climate Forecast System. *J. Climate*, **19**, 3483–3517, https://doi.org/10.1175/JCLI3812.1.

——, and Coauthors, 2014: The NCEP Climate Forecast System version 2. *J. Climate*, **27**, 2185–2208, https://doi.org/10.1175/JCLI-D-12-00823.1.

Schreck, C. J., III, L. Shi, J. P. Kossin, and J. J. Bates, 2013: Identifying the MJO, equatorial waves, and their impacts using 32 years of HIRS upper-tropospheric water vapor. *J. Climate*, **26**, 1418–1431, https://doi.org/10.1175/JCLI-D-12-00034.1.

Serra, Y. L., G. N. Kiladis, and M. F. Cronin, 2008: Horizontal and vertical structure of easterly waves in the Pacific ITCZ. *J. Atmos. Sci.*, **65**, 1266–1284, https://doi.org/10.1175/2007JAS2341.1.

Si, W., H. Liu, X. Zhang, and M. Zhang, 2021: Double intertropical convergence zones in coupled ocean-atmosphere models: Progress in CMIP6. *Geophys. Res. Lett.*, **48**, e2021GL094779, https://doi.org/10.1029/2021GL094779.

Song, X., and G. J. Zhang, 2019: Culprit of the eastern Pacific double-ITCZ bias in the NCAR CESM1.2. *J. Climate*, **32**, 6349–6364, https://doi.org/10.1175/JCLI-D-18-0580.1.

Straub, K. H., and G. N. Kiladis, 2002: Observations of a convectively coupled Kelvin wave in the eastern Pacific ITCZ. *J. Atmos. Sci.*, **59**, 30–53, https://doi.org/10.1175/1520-0469(2002)059<0030:OOACCK>2.0.CO;2.

——, and ——, 2003: Extratropical forcing of convectively coupled Kelvin waves during austral winter. *J. Atmos. Sci.*, **60**, 526–543, https://doi.org/10.1175/1520-0469(2003)060<0526:EFOCCK>2.0.CO;2.

Takayabu, Y. N., and T. Nitta, 1993: 3-5 day-period disturbances coupled with convection over the tropical Pacific Ocean. *J. Meteor. Soc. Japan*, **71**, 221–246, https://doi.org/10.2151/jmsj1965.71.2_221.

Wang, B., and H. Rui, 1990: Dynamics of the coupled moist Kelvin–Rossby wave on an equatorial β-plane. *J. Atmos. Sci.*, **47**, 397–413, https://doi.org/10.1175/1520-0469(1990)047<0397:DOTCMK>2.0.CO;2.

Wang, C., and G. Magnusdottir, 2005: ITCZ breakdown in three-dimensional flows. *J. Atmos. Sci.*, **62**, 1497–1512, https://doi.org/10.1175/JAS3409.1.

——, and ——, 2006: The ITCZ in the central and eastern Pacific on synoptic time scales. *Mon. Wea. Rev.*, **134**, 1405–1421, https://doi.org/10.1175/MWR3130.1.

Wang, C.-C., W.-L. Lee, Y.-L. Chen, and H.-H. Hsu, 2015: Processes leading to double intertropical convergence zone bias in CESM1/CAM5. *J. Climate*, **28**, 2900–2915, https://doi.org/10.1175/JCLI-D-14-00622.1.

Weller, E., K. Shelton, M. J. Reeder, and C. Jakob, 2017: Precipitation associated with convergence lines. *J. Climate*, **30**, 3169–3183, https://doi.org/10.1175/JCLI-D-16-0535.1.

Wheeler, M., and G. N. Kiladis, 1999: Convectively coupled equatorial waves: Analysis of clouds and temperature in the wavenumber–frequency domain. *J. Atmos. Sci.*, **56**, 374–399, https://doi.org/10.1175/1520-0469(1999)056<0374:CCEWAO>2.0.CO;2.

——, ——, and P. J. Webster, 2000: Large-scale dynamical fields associated with convectively coupled equatorial waves. *J. Atmos. Sci.*, **57**, 613–640, https://doi.org/10.1175/1520-0469(2000)057<0613:LSDFAW>2.0.CO;2.

Wilks, D. S., 2016: "The stippling shows statistically significant grid points": How research results are routinely overstated and overinterpreted, and what to do about it. *Bull. Amer. Meteor. Soc.*, **97**, 2263–2273, https://doi.org/10.1175/BAMS-D-15-00267.1.

Wodzicki, K. R., and A. D. Rapp, 2016: Long-term characterization of the Pacific ITCZ using TRMM, GPCP, and ERA-Interim. *J. Geophys. Res. Atmos.*, **121**, 3153–3170, https://doi.org/10.1002/2015JD024458.

Yang, W., and G. Magnusdottir, 2016: Interannual signature in daily ITCZ states in the east Pacific in boreal spring. *J. Climate*, **29**, 8013–8025, https://doi.org/10.1175/JCLI-D-16-0395.1.

Yin, B., and B. A. Albrecht, 2000: Spatial variability of atmospheric boundary layer structure over the eastern equatorial Pacific. *J. Climate*, **13**, 1574–1592, https://doi.org/10.1175/1520-0442(2000)013<1574:SVOABL>2.0.CO;2.

Yokoyama, C., and Y. N. Takayabu, 2012: Relationships between rain characteristics and environment. Part II: Atmospheric disturbances associated with shallow convection over the eastern tropical Pacific. *Mon. Wea. Rev.*, **140**, 2841–2859, https://doi.org/10.1175/MWR-D-11-00251.1.

Zhang, C., 2001: Double ITCZs. *J. Geophys. Res.*, **106**, 11 785–11 792, https://doi.org/10.1029/2001JD900046.

——, and M. Dong, 2004: Seasonality in the Madden–Julian oscillation. *J. Climate*, **17**, 3169–3180, https://doi.org/10.1175/1520-0442(2004)017<3169:SITMO>2.0.CO;2.

Zhang, X., H. Liu, and M. Zhang, 2015: Double ITCZ in coupled ocean–atmosphere models: From CMIP3 to CMIP5. *Geophys. Res. Lett.*, **42**, 8651–8659, https://doi.org/10.1002/2015GL065973.